

1 **Insights into carbonate environmental conditions in the Chukchi Sea**

2

3 Claudine Hauri¹, Brita Irving¹, Sam Dupont^{2,3}, Rémi Pagés¹, Donna D. W. Hauser¹, and Seth L.

4 Danielson⁴

5

6 ¹ International Arctic Research Center, University of Alaska Fairbanks, Fairbanks, AK 99775,

7 USA

8 ² Department of Biological and Environmental Sciences, University of Gothenburg,

9 Fiskebäckskil 45178, Sweden

10 ³ Radioecology Laboratory International Atomic Energy Agency (IAEA), Marine Laboratories,

11 Principality of Monaco

12 ⁴ College of Fisheries and Ocean Science, University of Alaska Fairbanks, Fairbanks, AK 99775,

13 USA

14

15 Correspondence email: chauri@alaska.edu

16 **Abstract**

17 Healthy Arctic marine ecosystems are essential to the food security and sovereignty, culture,
18 and wellbeing of Indigenous Peoples in the Arctic. At the same time, Arctic marine ecosystems
19 are highly susceptible to impacts of climate change and ocean acidification. While increasing
20 ocean and air temperatures and melting sea ice act as direct stressors on the ecosystem, they also
21 indirectly enhance ocean acidification, accelerating the associated changes in the inorganic
22 carbon system. Yet, much is to be learned about the current state and variability of the inorganic
23 carbon system in remote, high-latitude oceans. Here, we present time-series (2016-2020) of pH
24 and the partial pressure of carbon dioxide ($p\text{CO}_2$) from the northeast Chukchi Sea continental
25 shelf. The Chukchi Ecosystem Observatory includes a suite of subsurface year-round moorings
26 sited amid a biological hotspot that is characterized by high primary productivity and a rich
27 benthic food web that in turn supports coastal Iñupiat, whales, ice seals, walrus (*Odobenus*
28 *rosmarus*), and Arctic cod (*Boreogadus saida*). Our observations suggest that near-bottom
29 waters (33 m depth, 13 m above the seafloor) are a high carbon dioxide and low pH and
30 aragonite saturation state (Ω_{arag}) environment in summer and fall, when organic material from the
31 highly productive summer remineralizes. During this time, Ω_{arag} can be as low as 0.4. In winter,
32 when the site was covered by sea ice, pH was < 8 and Ω_{arag} remained undersaturated under the
33 sea ice. There were only two short seasonal periods with relatively higher pH and Ω_{arag} , which
34 we term ocean acidification relaxation events. In spring, high primary production from sea ice
35 algae and phytoplankton blooms led to spikes in pH ($\text{pH} > 8$) and aragonite oversaturation. In
36 late fall, strong wind driven mixing events that delivered low CO_2 surface water to the shelf also
37 led to events with elevated pH and Ω_{arag} . Given the recent observations of high rates of ocean
38 acidification, and sudden and dramatic shift of the physical, biogeochemical, and ecosystem

39 conditions in the Chukchi Sea, it is possible that the observed extreme conditions at the Chukchi
40 Ecosystem Observatory are deviating from carbonate conditions to which many species are
41 adapted.

42

43 **1. Introduction**

44 The quickly changing Arctic Ocean has climatic, societal, and geopolitical implications for
45 the peoples of the Arctic and beyond (Huntington et al., 2022). Arctic Indigenous Peoples are at
46 the forefront of this change and their food security, food sovereignty, culture, and ways of life
47 depend on healthy Arctic marine ecosystems (ICC, 2015). The Arctic is warming at a rate that is
48 up to four times that of the rest of the globe (Serreze and Barry, 2011; Serreze and Francis, 2006;
49 Rantanen et al., 2022). This phenomenon, called Arctic Amplification, is observed in air and sea
50 temperatures, has accelerated in recent years, and is expected to continue in the future (Rantanen
51 et al., 2022; Shu et al., 2022). Warming exerts a toll on sea ice extent, ice thickness, and the
52 duration of seasonal sea ice cover: ice is forming later in fall and retreating earlier in spring,
53 thereby increasing the length of the open water period (Stroeve et al., 2011; Serreze et al., 2016;
54 Wood et al., 2015; Stroeve et al., 2014). The lowest Arctic wide minimum sea ice extents were
55 recorded during the last 16 years of the 44 year-long satellite time-series (National Snow and Ice
56 Data Center).

57 At the same time, the Arctic Ocean is vulnerable to ocean acidification. Although oceanic
58 uptake of anthropogenic carbon dioxide (CO₂) increases oceanic CO₂ and decreases pH and
59 calcium carbonate (CaCO₃) saturation states of calcite (Ω_{calc}) and aragonite (Ω_{arag}) globally,
60 climate induced changes to riverine input, temperature, sea ice, and circulation are accelerating
61 the rate of ocean acidification in the Arctic Ocean like nowhere else in the world (Woosley and

62 Millero, 2020; Qi et al., 2022a; Yamamoto-Kawai et al., 2009; Orr et al., 2022; Semiletov et al.,
63 2016; Qi et al., 2017). Recent observational studies propose that freshening of the Arctic Ocean
64 due to increased riverine input may play an even greater role in acidifying the Arctic Ocean than
65 the uptake of anthropogenic CO₂ (Woosley and Millero, 2020; Semiletov et al., 2016). In
66 addition, the cold Arctic waters have naturally low concentrations of carbonate ions (CO₃²⁻) and
67 are therefore closer to aragonite undersaturation ($\Omega_{\text{arag}} < 1$) than more temperate waters (Orr,
68 2011; Sarmiento and Gruber, 2006), which leads to the chemical dissolution of free aragonitic
69 CaCO₃ structures (Bednaršek et al., 2021). Because of the naturally low concentrations of CO₃²⁻,
70 such high latitude waters have a lower capacity to take up anthropogenic CO₂ and buffer these
71 changes (Orr, 2011). As a result, concentrations of hydrogen ions (H⁺) increase and pH decreases
72 faster in the Arctic than in the tropics, for example.

73 In the Pacific Arctic, the Chukchi shelf waters have warmed by 0.45 °C decade⁻¹ since 1990,
74 triple the rate since the beginning of the data record in 1922 (Danielson et al., 2020). Direct
75 observations of the inorganic carbon dynamics of the Chukchi Sea are mostly limited to June
76 through November because of the region's remoteness and accessibility during sea ice covered
77 months. Summertime profiles across the Chukchi Sea show steep vertical gradients in inorganic
78 carbon chemistry (Bates, 2015; Bates et al., 2009; Pipko et al., 2002; Mathis and Questel, 2013).
79 Surface waters have a low partial pressure of carbon dioxide ($p\text{CO}_2$) as a result of high primary
80 production after sea ice retreat, leading to aragonite supersaturated conditions, with $\Omega_{\text{arag}} > 2$
81 (Bates, 2015; Bates et al., 2009). In areas with sea ice melt or riverine freshwater influence, Ω_{arag}
82 tends to be lower and at times undersaturated (Bates et al., 2009; Yamamoto-Kawai et al., 2009).
83 At the same time, $p\text{CO}_2$ values near the seafloor are around 1000 μatm as a result of organic
84 matter, leading to summertime aragonite undersaturation (Mathis and Questel, 2013; Pipko et al.,

85 2002; Bates, 2015). Between September and November, continuous measurements from within a
86 few meters of the surface suggest a mosaic of $p\text{CO}_2$ levels between ~ 200 to $600 \mu\text{atm}$, likely due
87 to patchy wind-induced mixing entraining high- CO_2 waters from depth into the surface mixed
88 layer (Hauri et al., 2013). Yamamoto-Kawai et al. (2016) used mooring observations of S, T, and
89 apparent oxygen utilization to estimate dissolved inorganic carbon (DIC), total alkalinity (TA),
90 and Ω_{arag} in bottom waters at their mooring site in the Hope Valley in the southwestern Chukchi
91 Sea to give first insights into year round variability of the inorganic carbon system. They found
92 slightly less intense aragonite undersaturation in spring and winter compared to summer, with a
93 net undersaturation duration of 7.5-8.5 months per year.

94 The Chukchi Ecosystem Observatory (CEO) is situated in a benthic hotspot (Figure 1) where
95 high primary production supports rich and interconnected benthic and pelagic food webs
96 (Grebmeier et al., 2015; Moore and Stabeno, 2015). The benthos is dominated by calcifying
97 bivalves, polychaetes, amphipods, sipunculids, echinoderms and crustaceans (Grebmeier et al.,
98 2015; Blanchard et al., 2013). Benthic foraging bearded seals (*Erignathus barbatus*), walrus
99 (*Odobenus rosmarus divergens*), gray whale (*Eschrichtius robustus*), and seabirds feed on these
100 calcifiers during the open water season (Kuletz et al., 2015; Jay et al., 2012; Moore et al., 2022).
101 The CEO site, located on the southern flank of Hanna Shoal, is a region of reduced stratification
102 (relative to other sides of the shoal) that likely alternately feels the effects of differing flow
103 regimes located to the west and to the east (Fang et al., 2020). Consequently, the site exhibits
104 relatively weaker currents (Tian et al., 2021) and so is conducive to deposition of sinking organic
105 matter that in turn feeds the local benthos (Grebmeier et al., 2015). Prolonged open-water
106 seasons during periods of high solar irradiance, in combination with an influx of new nutrients
107 and wind mixing, are likely enhancing primary and secondary production as well as advection of

108 zooplankton (Lewis et al., 2020; Arrigo and van Dijken, 2015; Wood et al., 2015). These
109 physical processes in turn fuel keystone consumers such as Arctic cod (*Boreogadus saida*) and
110 upper trophic level ringed seals (*Phoca hispida*), beluga (*Delphinapterus leucas*) and bowhead
111 whales (*Balaena mysticetus*) as well as predatory polar bears (*Ursus arctos*) and Indigenous
112 People who rely on the marine ecosystem for traditional and customary harvesting (Huntington
113 et al., 2020).

114 Perturbation of the seawater carbonate system associated with ocean acidification and
115 climate change can have significant physiological and ecological consequences for marine
116 species and ecosystems (Doney et al., 2020). All parameters of the carbonate system (pH, $p\text{CO}_2$,
117 Ω_{arag} , concentrations of HCO_3^- , CO_3^{2-} , etc.) have the potential to affect the physiology of marine
118 organisms while a change in the saturation state (Ω) can lead to the dissolution of unprotected or
119 “free” CaCO_3 structures. Recent work has highlighted the importance of local adaptation to the
120 present environmental variability as a key factor driving species sensitivity to ocean acidification
121 (Vargas et al., 2017, 2022). As carbonate chemistry conditions vary enormously between
122 regions, marine organisms are naturally exposed to different selective pressures and can evolve
123 different strategies to cope with low pH or Ω , or high $p\text{CO}_2$. For example, the deep-sea mussel
124 *Bathymodiolus brevior* living around vents at 1600 m depths is capable of precipitating calcium
125 carbonate at pH ranging between 5.36 and 7.30 and highly undersaturated waters (Tunnicliffe et
126 al., 2009). The response to changes in the carbonate chemistry is also modulated by other
127 environmental drivers such as temperature or food availability (e.g. Thomsen et al., 2013;
128 Breitberg et al., 2015). Consequently, no absolute or single threshold is expected for ocean
129 acidification (e.g., Bednaršek et al., 2021) and a pre-requisite to assessing the impact on any
130 biota is the monitoring at a short temporal scale to characterize the present environmental niche.

131 When it comes to future impacts, the more intense and faster the changes associated with ocean
132 acidification, the more adverse associated biological impacts are expected (Vargas et al. 2017,
133 2022). As a result, it is anticipated that Arctic marine waters that are experiencing widespread
134 and rapid ocean acidification will potentially undergo severe negative ecosystem impacts
135 (AMAP 2018).

136 Here, we present satellite sea ice coverage data and four years of nearly continuous salinity,
137 temperature, and $p\text{CO}_2$ data, accompanied by pH, nitrate (NO_3), dissolved oxygen (O_2), and
138 chlorophyll fluorescence data for some of the time (Table 1, Figures 2 and 3). We developed an
139 empirical equation for estimating pH from moored $p\text{CO}_2$, temperature, and salinity and evaluated
140 it using discrete samples collected across the Chukchi Sea, Bering Sea, and Beaufort Sea. Our
141 timeseries allow us to assess the seasonal and interannual variability and controls of the
142 inorganic carbon system in the Chukchi Sea between 2016 and 2020 and characterize the
143 chemical conditions experienced by organisms. We discuss our observations in terms of
144 progressing acidification and implications to organisms in the Chukchi Sea region.

145

146 **2. Materials and Methods**

147 **2.1 The Chukchi Ecosystem Observatory (CEO)**

148 The Chukchi Sea is a shallow shelf sea with maximum depths < 50 m. It is largely a
149 unidirectional inflow shelf system with Pacific origin water entering the Chukchi Sea through the
150 Bering Strait and advecting north into the Arctic Ocean (Carmack and Wassmann, 2006). The
151 CEO ($71^{\circ}36' \text{ N}$, $161^{\circ}30' \text{ W}$, Figure 1, Hauri et al., 2018) is located along the pathway of waters
152 flowing through Bering Strait (Fang et al., 2020) and thence from the west of Hanna Shoal
153 toward Barrow Canyon to the south, although the wind can also drive waters from the east over

154 the observatory site (Fang et al., 2020). From both shipboard and moored acoustic Doppler
155 current profiler records, the south side of Hanna Shoal mean flow is characterized by a weak
156 southward-directed current (Tian et al., 2021).

157 The observatory consists of oceanographic moorings that sample year-round, equipped with a
158 variety of sensors that measure sea ice cover and thickness (Sandy et al., 2022), light, currents,
159 waves, salinity, temperature, concentrations of dissolved oxygen, nitrate, and particulate matter,
160 pH, $p\text{CO}_2$, chlorophyll fluorescence, zooplankton abundance and vertical migration (Lalande et
161 al., 2021, 2020), the presence of Arctic cod and zooplankton (Gonzalez et al., 2021), and the
162 vocalizations of marine mammals. During some years, the observatory included a third mooring,
163 an experimental “freeze-up detection mooring”, which transmitted real-time data of conductivity
164 and temperature throughout the water column until sea ice formation. The primary moorings
165 stretch from the seafloor at 46 m to about 33 m depth, designed to avoid collisions with ice keels.
166 Pressure sensors at the top of the moorings show less than ± 1 m of excursion of the moored
167 sensor package from its deployment mean depth in any given year, indicating that mooring blow-
168 over or diving is not the cause of any observed large variability. Description of the CEO and lists
169 of sensors deployed at the site can be found in Danielson et al. (2017) and Hauri et al., (2018).
170 For this study we focus on the inorganic carbon system and its controlling mechanisms.

171

172 **2.2 $p\text{CO}_2$**

173 We used a CONTROS HydroC CO_2 sensor (4H-Jena Engineering GmbH, Kiel, Germany) to
174 measure $p\text{CO}_2$. The Contros HydroC CO_2 sensor was outfitted with a pump (SBE 5M, Sea-Bird
175 Electronics) that flushes ambient seawater against a thin semi permeable membrane, which
176 serves as equilibrator for dissolved CO_2 between the ambient seawater and the headspace of the

177 sensor. Technical details about the sensor and its performance are described in Fietzek et al.
178 (2014), who estimated sensor accuracy to be better than 1% with postprocessing.

179 A HydroC CO₂ sensor has been deployed at the CEO site since 2016. In all deployments,
180 except 2016, HydroC CO₂ sensors were post-calibrated. The lack of post-calibration in 2016 is
181 not expected to negatively affect data quality because a battery failure resulted in data returns
182 only over the first 3 months (August through November). Following a zero interval where the
183 gas was pumped through a soda lime cartridge to create a zero-signal reference with respect to
184 CO₂, and subsequent flush interval to allow CO₂ concentrations to return to ambient conditions,
185 measurements were taken in a burst fashion every 12 or 24 hours depending on deployment year
186 (Table 1). Average *p*CO₂ values are reported as the mean of the measure interval (Table 1) with
187 standard uncertainty (Equation 1) defined following best practices (Orr et al., 2018) and where
188 the random component is the standard deviation of the mean, and the systematic components
189 include sensor accuracy and estimated error of the regression during calibration.

190

$$u = \sqrt{u_{\text{systematic}}^2 + u_{\text{random}}^2} \quad (1)$$

191 More than 96% of the time, the relative uncertainty of the *p*CO₂ data met the weather data
192 quality goal, defined as 2.5% by the Global Ocean Acidification Observing Network (GOA-ON,
193 Newton et al., 2015).

194 HydroC CO₂ data were processed using Jupyter notebook scripts developed by 4H-Jena
195 Engineering GmbH using pre- and post-calibration coefficients interpolated with any change in
196 the zero-signal reference over the deployment (Fietzek et al., 2014). Further processing using in-
197 house MATLAB scripts included removal of outliers, calculation of the average *p*CO₂, and
198 calculation of uncertainty estimates for each measure interval.

199

200 **2.3 pH**

201 A SeapHOx sensor (Satlantic SeaFET™ V1 pH sensor integrated with Sea-Bird Electronics

202 SBE 37-SMP-ODO) was used to concurrently measure pH, salinity, temperature, pressure, and

203 oxygen (Martz et al., 2010). A SeapHOx was deployed at CEO in 2016, 2017, and 2018. No

204 SeapHOx was deployed in 2019 or 2020 due to supply chain delays and communication issues at

205 sea. Unfortunately, measured pH ($\text{pH}_{\text{SeaFET}}$) from the 2016 and 2018 SeapHOx deployments

206 were unusable due to high levels of noise in both the internal and external electrodes. In short,

207 we only have usable pH data between August 2017 and August 2018.

208 $\text{pH}_{\text{SeaFET}}$ data were excluded during a 14-day conditioning period following deployment and

209 were processed with post-calibration corrected temperature and salinity from the SBE37

210 following Bresnahan et al. (2014) using voltage from the external electrode (V_{ext}), and pH_{Vext}

211 (pH calculated from the external electrode of the SeaFET) from an extended period of low

212 variability (18 February 2018). Despite the availability of discrete data from one calibration cast

213 (Cross et al., 2020b; Table 2), pH_{Vext} was used as the single calibration point (Bresnahan et al.,

214 2014) for a variety of reasons: 1) high variability of $\text{pH}_{\text{SeaFET}}$ (0.0581 pH units) straddling a 12

215 hour window around the discrete sample collection time, 2) high temporal and spatial variability

216 often seen in the Chukchi Sea, and 3) the discrete pH sample was within the published SeaFET

217 accuracy of 0.05 (Table 2, Figure S1). $\text{pH}_{\text{SeaFET}}$ values are reported as the mean of the measure

218 interval (Table 1) and standard uncertainty is calculated with Equation 1 with the standard

219 deviation of the average (random), and the SeaFET accuracy (systematic). Data handling and

220 processing were done using in-house MATLAB scripts. pH is reported in total scale and at *in*

221 *situ* temperature for the entirety of this paper.

222

223 **2.4 Nitrate**

224 NO₃ measurements were from a Submersible Ultraviolet Nitrate Analyzer (SUNA) V2 by
225 Sea-Bird Scientific. The SUNA is an *in situ* ultraviolet spectrophotometer designed to measure
226 the concentration of nitrate ions in water. SUNA V2 data were processed using a publicly
227 available toolbox (Hennon et al., 2022; Irving, 2021) with QA/QC steps that included thermal
228 and salinity corrections (Sakamoto et al., 2009), assessment of spectra and outlier removal based
229 on spectral counts (Mordy et al., 2020), and concentration adjustments (absolute offset and linear
230 drift) based on pre-deployment and post-recovery reference measurements of zero concentration
231 (DI) water and a nitrate standard and, when available, nutrient samples taken from Niskin bottles
232 near the mooring site (e.g. Daniel et al., 2020).

233

234 **2.5 CTD and Oxygen**

235 Two CTDs were deployed on the CEO mooring near the HydroC CO₂ depth. The main
236 pumped Sea-Bird SeaCAT (SBE16) has been deployed on the CEO mooring around 33 m depth
237 since 2014. A pumped SBE43 oxygen sensor was deployed with the SBE16 during the 2015-
238 2016, 2017-2018, and 2019-2020 deployments but only data returns from the 2017-2018
239 deployment is discussed briefly in this manuscript (Figure S2).

240 The other pumped CTD was a Sea-Bird MicroCAT (SBE37-SMP-ODO), which was
241 integrated with an optical dissolved oxygen sensor (SBE63; Figure S2), and the SeaFET pH
242 sensor within the SeapHOx instrument. The SeapHOx was deployed in fall 2016, 2017, and
243 2018. The SBE37-SMP-ODO did not record any CTD or oxygen data during the 2016
244 deployment and only recorded CTD and oxygen data between August and November 3 in 2018
245 due to battery failure.

246 Processing of these data included temperature and conductivity correction using pre- and
247 post-calibration data following Sea-Bird Application Note 31 and oxygen correction using pre-
248 and post-calibration data following Sea-Bird Module 28. Oxygen was converted from ml/l to
249 $\mu\text{mol/kg}$ following Bittig et al. (2018). Density and practical salinity were calculated using the
250 TEOS-10 GSW Oceanographic Toolbox (McDougall and Baker, 2011).

251 Differences between the two oxygen sensors (SBE43 and SBE63) of approximately 145 to
252 265 $\mu\text{mol/kg}$ were observed over the 2017-2018 deployment, and both moored sensors had
253 varying offsets compared to nearby casts (Figure S2). Therefore, only relative oxygen values
254 from the freshly calibrated SBE63 are discussed in this paper.

255 The freeze-up detection mooring (Figure 6) consisted of four Sea-Bird SBE 37 inductive
256 modem CTD sensors that transmitted in real time hourly temperature, salinity, and pressure data
257 via the surface float from four subsurface depths (8, 20, 30, and 40 m; Hauri et al., 2018).

258

259 **2.6 Development of empirical relationship to estimate pH**

260 Empirical relationships for estimating water column pH have been developed for regions
261 spanning southern, tropical, temperate and Arctic biomes, using a variety of commonly measured
262 parameters (e.g., $\text{pH}(\text{S}, \text{T}, \text{NO}_3, \text{O}_2, \text{Si})$ Carter et al 2018; $\text{pH}(\text{O}_2, \text{T}, \text{S})$ Li et al., 2016; $\text{pH}(\theta, \text{O}_2)$
263 Watanabe et al., 2020; $\text{pH}(\text{NO}_3, \text{T}, \text{S}, \text{P})$ and $\text{pH}(\text{O}_2, \text{T}, \text{S}, \text{P})$ Williams et al., 2016; $\text{pH}(\text{O}_2, \text{T})$
264 Alin et al., 2012; $\text{pH}(\text{O}_2, \text{T})$ and $\text{pH}(\text{NO}_3, \text{T})$ Juranek et al., 2009). Given the tight coupling
265 between the concentration of H^+ and concentration of CO_2 solution, an empirical relationship for
266 estimating surface pH from $p\text{CO}_2$ was developed by the National Academies of Sciences,
267 Engineering and Medicine (2017) appendix F. Licker et al. (2019) used this empirical
268 relationship to calculate the global average surface ocean pH and found it represented the

269 relationship for surface water temperatures spanning 5°C to 45°C. Here, we take a similar
270 approach but extend it to water column pH in our cold region using temperature (T) and salinity
271 (S) as additional proxy parameters (Equation 2).

$$272 \quad pH^{est} = \alpha_0 + \alpha_1 \log(pCO_2) + \alpha_2 T + \alpha_3 S \quad (2)$$

273 Where pH^{est} is the estimated value of water column pH, pCO_2 is from the HydroC, and T and S
274 are from the SBE16, and all α ($\alpha_0 = 10.4660$, $\alpha_1 = -0.4088$, $\alpha_2 = 0.0013$, $\alpha_3 = -0.0001$) terms are
275 model-estimated coefficients determined using MATLAB's multiple linear regression algorithm
276 *regress.m* (Chatterjee and Hadi, 1986). After interpolating pH_{SeaFET} (Figure 4, red dots) to the
277 pCO_2 timestamp, the algorithm was trained over an arbitrarily chosen 180-day period
278 (15/9/2017-14/3/2018, Figure 4, dashed box). An uncertainty of 0.0525 for pH^{est} (Figure 3 and
279 Figure S1, gray shading) was determined with Equation 1, where the RMSE (the uncertainty in
280 the estimation) over the entire pH_{SeaFET} timeseries is the random component and the published
281 accuracy of the SeaFET is the systematic component (since the algorithm was trained with
282 pH_{SeaFET}). The algorithm cross-validation and evaluation are discussed in section 3.1. Unless
283 explicitly defined otherwise, observations of pH refer to pH^{est} for the remainder of this paper.

284

285 **2.7 Carbonate system calculations**

286 Moored data were collected at different sample intervals (Table 1) and were linearly
287 interpolated to the HydroC CO₂ timestamp to enable further calculations. TA, DIC, and Ω_{arag}
288 (Figure 11 a & b and Figure 3d) were calculated based on measured pCO_2 , S, T, and pressure (P)
289 and algorithm-based pH (pH^{est}). Due to a lack of data, nutrient concentrations (Si, PO₄, NH₄,
290 H₂S) were assumed to be negligible in the CO2SYS calculations (e.g. deGrandpre et al., 2019;
291 Vergara-Jara et al., 2019; Islam et al., 2017). pH^{est} was used in lieu of pH_{SeaFET} to allow for

292 calculations over the whole $p\text{CO}_2$ record and due to erroneously large variability of DIC and TA
293 when $\text{pH}_{\text{SeafET}}$ was used as an input parameter (Raimondi et al., 2019; Cullison-Gray et al.,
294 2011). The pH - $p\text{CO}_2$ input pair leads to large, calculated errors in DIC and TA (Raimondi et al.,
295 2019; Cullison-Gray et al., 2011) due to strong covariance between the two parameters (both
296 temperature and pressure dependent). Cullison-Gray et al. (2011) attributed unreasonably large
297 short-term variability in calculated TA and DIC to temporal or spatial measurement mismatches
298 between input pH and $p\text{CO}_2$ parameters and found that appropriate filtering alleviated noise
299 spikes. By using pH^{est} , which by the nature of its definition is well correlated to $p\text{CO}_2$, we are
300 eliminating some of these spurious noise spikes. We show Ω_{arag} calculated from $\text{pH}_{\text{SeafET}}$ - $p\text{CO}_2$
301 (Figure 3d, red line) because it is less sensitive to calculated errors as it accounts for a small
302 portion of the total CO_2 in seawater (Cullison-Gray et al., 2011).

303 All inorganic carbon parameters were calculated using CO2SYSv3 (Sharp et al., 2023; Lewis
304 and Wallace, 1998) with dissociation constants for carbonic acid of Lueker et al. (2000),
305 bisulfate of Dickson (1990), hydrofluoric acid of Perez and Fraga (1987), and the boron-to-
306 chlorinity ratio of Lee et al. (2010). Sulpis et al. (2020) found that the carbonic acid dissociation
307 constants of Lueker et al. (2000) may underestimate $p\text{CO}_2$ in cold regions (below $\sim 8^{\circ}\text{C}$), and
308 therefore overestimate pH and CO_3^{2-} . However, we choose to use Lueker et al. (2000) because
309 they are recommended (Dickson et al., 2007; Woosley, 2021), continue to be the standard (Jiang
310 et al., 2021; Lauvset et al., 2021), and are commonly used at high latitudes (Duke et al., 2021;
311 Raimondi et al., 2019; Woosley et al., 2017). Furthermore, the difference between DIC
312 calculated from pH^{est} and $p\text{CO}_2$ and discrete samples interpolated to moored instrument depth
313 ranged from 266 to -195 $\mu\text{mol/kg}$ using the k1 k2 of Sulpis et al. (2020), compared to -38 to -7
314 $\mu\text{mol/kg}$ using Lueker et al. (2000).

315

316 **2.8 Sea ice concentration**

317 Sea ice concentration at the observatory site was taken from the National Snow and Ice Data
318 Center (NSIDC; DiGirolamo et al., 2022). Latitude and longitude coordinates were converted to
319 NSIDC's EASE grid coordinate system (Brodzik and Knowles, 2002) and the 25-km gridded
320 data were bilinearly interpolated to calculate sea ice concentration at the CEO site. Low sea ice is
321 defined by < 15 % sea ice coverage per grid cell.

322

323 **2.9 Estimation of model-based ocean acidification trend**

324 Model results were obtained from historical simulations of five different global Earth System
325 Models: 1) GFDL-CM4 (Silvers et al., 2018), 2) GFDL-ESM4 (Horowitz et al., 2018), 3) IPSL-
326 CM6A-LR-INCA (Boucher et al., 2020), 4) CNRM-ESM2-1 (Seferian, 2019), and 5) Max Plank
327 Earth System Model 1.2 (MPI-ESM1-2-LR, Wieners et al., 2019) that are part of the Coupled
328 Model Intercomparison Project Phase 6 (CMIP6). Each simulation was used to calculate the
329 annual trend of aragonite saturation state and pH at the closest depth and grid cell to the CEO
330 mooring.

331

332 **3. Results**

333 In the following, we will evaluate the pH algorithm (section 3.1), analyze the large
334 variability patterns (sections 3.2 and 3.3), and then take a closer look at the data from 2020 since
335 the seasonal cycle was different in 2020 than in previous years (section 3.4).

336

337 **3.1 pH algorithm**

338 The algorithm estimated pH data from the CEO site reasonably well and within the weather
339 uncertainty goal as defined by Newton et al. (2015) most of the time. As a first step, pH^{est}
340 consistency was assessed through cross-validation (Figure 5) using the test dataset (outside the
341 training period, $r^2 = 0.9666$, RMSE = 0.166) and across the whole timeseries ($r^2 = 0.9598$, RMSE
342 = 0.0161, $p < 0.0001$, Figure 5). Observed high frequency spikes in $\text{pH}_{\text{SeaFET}}$ (Figure 4, red dots;
343 Figure 5d, red line) were not captured by the HydroC $p\text{CO}_2$ sensor (sampling frequency of 12 h)
344 and as a result, are not reproduced in the pH^{est} timeseries. Throughout the $\text{pH}_{\text{SeaFET}}$ timeseries,
345 pH^{est} overestimates $\text{pH}_{\text{SeaFET}}$ by a mean of 0.0008 and median of 0.0039. Since pH^{est} generally
346 overestimates $\text{pH}_{\text{SeaFET}}$ (mean difference of 0.0008), we assume that Ω_{arag} is also somewhat
347 overestimated throughout this manuscript. Discrete water samples were used as reference values
348 to evaluate the algorithm at the CEO site (Table 2) and were found to be within the pH^{est}
349 uncertainty (Figure S1).

350 An independent verification of our algorithm was done using discrete data collected from the
351 Bering Sea to the Arctic Ocean on four research cruises in 2020, 2019, 2018, and 2017 (Figure
352 6d; Monacci et al., 2022; Cross et al., 2021; 2020a; 2020b), henceforth called the DBO dataset.
353 Samples collected from deeper than 500 m below the surface or flagged as questionable or bad
354 were excluded from this analysis. pH and $p\text{CO}_2$ were calculated from 1275 discrete samples
355 analyzed for TA, DIC, silicate, phosphate, and ammonium (except when silicate, phosphate, and
356 ammonium were assumed to be negligible for the 327 samples from SKQ202014S; Monacci et
357 al., 2022) using CO2SYSv3 (Sharp et al., 2023; section 2.7 for details) and are referred to as
358 $\text{pH}^{\text{disc}}_{\text{calc}}$ and $p\text{CO}_2^{\text{disc}}_{\text{calc}}$, respectively. $\text{pH}^{\text{disc}}_{\text{est}}$ was based on discrete water samples and
359 calculated using Equation 2 and was fit to $\text{pH}^{\text{disc}}_{\text{calc}}$ using a linear regression ($r^2 = 0.9975$, RMSE
360 = 0.0078, $p\text{-value} < 0.0001$; Figure 6 a – c). Mean and median differences between $\text{pH}^{\text{disc}}_{\text{calc}}$ and

361 $\text{pH}^{\text{disc}}_{\text{est}}$ were zero and 0.0022, respectively, with largest anomalies observed at lower salinities
362 (Figure 6c). Absolute differences between $\text{pH}^{\text{disc}}_{\text{est}}$ and $\text{pH}^{\text{disc}}_{\text{cal}}$ over the salinity range observed
363 at the CEO site (30.87 to 33.93) fall within the weather data quality goal (Newton et al., 2015)
364 98.7% of the time with maximum absolute differences < 0.03 . The uncertainty of 0.0154 for
365 $\text{pH}^{\text{disc}}_{\text{est}}$ was determined using Equation 1, where the mean combined standard uncertainty (u_c)
366 for $\text{pH}^{\text{disc}}_{\text{calc}}$ (0.0133; Orr et al., 2018) was the systematic component, and the regression RMSE
367 was the random component.

368 Empirical relationships for estimating water column pH that rely on dissolved oxygen often
369 ignore surface waters to limit biases due to decoupling the stoichiometry of the $\text{O}_2:\text{CO}_2$
370 relationship due to air-sea gas exchange (e.g. Juranek et al., 2011; Alin et al., 2012; Li et al.,
371 2016). We see evidence of this bias in our algorithm at low salinity (Figure 6c) and low $p\text{CO}_2$
372 (not shown) when compared with the DBO dataset samples collected across the Arctic and from
373 the surface to 500 m, with $\text{pH}^{\text{disc}}_{\text{est}}$ overestimating $\text{pH}^{\text{disc}}_{\text{calc}}$ by a maximum of 0.049. If depth is
374 restricted to between 30 and 500 m when evaluating the algorithm with the DBO dataset,
375 algorithm performance improves ($r^2 = 0.9990$, RMSE = 0.0055, p-value < 0.0001 ; not shown)
376 and the maximum $\text{pH}^{\text{disc}}_{\text{est}}$ overestimates $\text{pH}^{\text{disc}}_{\text{calc}}$ by 0.022.

377

378 **3.2 Relaxation events**

379 The sub-surface waters at the CEO site comprise a high $p\text{CO}_2$, low pH, and low Ω_{arag}
380 environment, with mean values of $p\text{CO}_2^{\text{mean}} = 538 \pm 7 \mu\text{atm}$, $\text{pH}^{\text{mean}} = 7.91 \pm 0.05$, $\Omega_{\text{arag}}^{\text{mean}} =$
381 0.94 ± 0.23 across the full data record (Figure 3 b - d). In the following we will focus on spikes
382 of high pH and Ω_{arag} and low $p\text{CO}_2$ that occur in spring (May-June) and fall (September-
383 December); we define these spikes as relaxation events (see discussion for justification of term).

384 Spring: Springtime relaxation events at 33 m depth that exhibit relatively higher pH and
385 Ω_{arag} and lower $p\text{CO}_2$ compared to the overall mean, are likely consequences of photosynthetic
386 activity during sea ice break-up (Figures 2 and 3). In June of 2019 and 2020, near bottom pH and
387 Ω_{arag} spiked to > 8.17 and > 1.5 , respectively, while $p\text{CO}_2$ dropped to $< 286 \mu\text{atm}$. Ω_{arag} remained
388 oversaturated and pH was greater than 8.0 for nearly all of June in 2018. In 2019, the relaxation
389 event was less sustained, with only four short (2-6 day-long) events of relatively higher pH and
390 $\Omega_{\text{arag}} > 1$ in June. In both years, chlorophyll fluorescence spiked and either O_2 increased (in
391 2018) or NO_3 decreased (in 2019), which are signs of photosynthetic activity and primary
392 production.

393 Fall: The relaxation events in fall were characterized by large and sudden drops in $p\text{CO}_2$,
394 abrupt increases in pH and Ω_{arag} , and considerable interannual variability in their timing. Unlike
395 the relaxation events observed in spring, we attribute these fall relaxation events to wind-induced
396 physical mixing. To examine the controlling mechanisms causing these abrupt relaxation events
397 in fall, we will start with using water column salinity and temperature data from a freeze-up
398 detection buoy (Hauri et al., 2018) that was deployed in summer 2017 approximately 1 km away
399 from the biogeochemical mooring. The freeze-up detection mooring provided temperature and
400 salinity measurements every 7 meters throughout the water column from the time of its
401 deployment in mid-August until freeze-up. Data from the freeze-up detection mooring suggest
402 that warmer and fresher water from the upper water column gets periodically entrained down to
403 the location of the biogeochemical sensor package at 33 m depth, leading to enhanced variability
404 of density in August and September (Figure 7). Fluctuations of the pycnocline associated with
405 the passage of internal waves could also elevate signal variances. During this time $p\text{CO}_2$ often
406 decreased to or below atmospheric levels and pH sporadically reached values > 8 . At the end of

407 September, a strong mixing event (with coincident strong surface winds) homogenized the water
408 column from the surface down to the location of the sensor package and caused a sudden
409 temperature increase from 0.4 °C to 3.9 °C (Figure 7c and 8a). At the same time, $p\text{CO}_2$ (Figure
410 7b and 8) decreased from 590 to 308 μatm . This suggests that warm and low CO_2 surface water
411 mixed with CO_2 -rich subsurface water and led to a sustained relaxation period that subsequently
412 lasted until mid-November. Another mixing event further eroded the water column stratification
413 and replaced subsurface water with colder and fresher water (ice melt) from the surface at the
414 end of October. This second large mixing event did not lead to large changes in $p\text{CO}_2$, pH, and
415 Ω_{arag} .

416 Salinity and temperature records from the biogeochemical mooring at 33 m depth also
417 suggest fall season mixing events in all other years, when increases in temperature coincide with
418 decreases in $p\text{CO}_2$ (Figure 8). For example, two mixing events shaped the carbonate chemistry
419 evolution in fall 2018. $p\text{CO}_2$ decreased from 915 μatm to around 565 μatm and Ω_{arag} increased to
420 0.9 as temperature increased and salinity decreased in early September (Figures 2 and 8). $p\text{CO}_2$
421 then increased to 1160 μatm in late October, before decreasing to 385 μatm at the beginning of
422 November, causing a spike in Ω_{arag} to 1.34. At the same time, salinity decreased by 1 unit,
423 suggesting a strong mixing event. Throughout November 2018, $p\text{CO}_2$ oscillated between 344 and
424 757 μatm and salinity between 31.01 and 32.97, hinting at additional mixing.

425 Similarly, an early mixing event in 2019 decreased $p\text{CO}_2$ to 352 μatm at the beginning of
426 September. Short-term variability in $p\text{CO}_2$ with maximum levels of up to 855 μatm and
427 minimum values below 300 μatm , variable temperature and salinity, and sporadic aragonite
428 oversaturation events point to mixing through mid-September. At the end of October, a large
429 mixing event homogenized the water column, accompanied by a decline of salinity by >1 unit,

430 increase of temperature to 4 °C, and decrease of $p\text{CO}_2$ from 565 μatm to below 400 μatm . In a
431 similar fashion to 2018, this fall mixing event was followed by a month-long period of large
432 variability of $p\text{CO}_2$, salinity, pH, and Ω_{arag} , leading to short and sporadic aragonite oversaturation
433 events in November, and sustained oversaturation in December.

434

435 **3.3 Sustained periods of low pH and Ω_{arag} , and high $p\text{CO}_2$**

436 Waters at 33 m depth at the CEO site were most acidified during the sea ice free periods
437 until mixing events entrained surface waters to the sensor depth (section 3.2). pH and Ω_{arag}
438 started to gradually decrease from their maximum levels ($\Omega_{\text{arag_max}} = 1.65$, $\text{pH}_{\text{max}} = 8.19$) at the
439 beginning of June in 2018 to their annual low at the beginning of November ($\Omega_{\text{arag_min}} = 0.47$,
440 $\text{pH}_{\text{min}} = 7.58$, Figure 3 d and c). In November, the waters were also undersaturated with regards
441 to calcite (not shown) and $p\text{CO}_2$ peaked at 1159 μatm (Figure 3b). Dissolved oxygen decreased
442 by about 400 $\mu\text{mol kg}^{-1}$ between July and October, when the sensor stopped working properly.
443 The decrease of dissolved oxygen suggests remineralization of organic material. The decrease of
444 pH, Ω_{arag} , O_2 and increase of $p\text{CO}_2$ was briefly interrupted by a strong mixing event in
445 September, which entrained warmer, fresher, and CO_2 -poorer water down to 33 m depth (section
446 3.2, Figure 8). The 2019 observations paint a similar picture of remineralization during the
447 summer months, as the $p\text{CO}_2$ increase and pH and Ω_{arag} decreases were accompanied by an NO_3^-
448 increase.

449 $p\text{CO}_2$ steadily increased and pH and Ω_{arag} decreased during the sea ice covered periods
450 (Figures 8). pH was < 8 and Ω_{arag} remained undersaturated under the sea ice. At the same time,
451 NO_3^- slowly increased and O_2 decreased, which points to slow organic matter remineralization
452 (Figure 9). Short-term variability in $p\text{CO}_2$, especially in January of all three observed years, was

453 also reflected in salinity, O₂ and NO₃ (Figure 9) and could be attributed to advection, as the CEO
454 site is adjacent to contrasting regimes of flow and hydrographic properties (Fang et al., 2020).

455

456 **3.4 Spring and summer of 2020 were different**

457 The seasonal cycle in 2020 strongly contrasted with the previous observed years. *p*CO₂
458 gradually increased by roughly 200 μ atm throughout the sea ice covered months to 650 μ atm
459 when sea ice started to retreat at the beginning of July. By the end of July, *p*CO₂ doubled and
460 increased to 1389 μ atm, which is the highest *p*CO₂ level recorded in this timeseries. The peak of
461 *p*CO₂ was accompanied by an increase in salinity of 0.5 while temperature did not change,
462 suggesting the influence of advection. At the beginning of August, *p*CO₂ dropped to 536 μ atm
463 and then oscillated around 600 μ atm through much of August before returning to around 900
464 μ atm for the next month. Similarly, pH decreased to 7.5 at the end of July and then oscillated
465 around 7.85, while Ω_{arag} dropped to 0.37, and oscillated around 0.85. The steep drop and
466 oscillation of *p*CO₂ was reflected in NO₃, suggesting that primary production and
467 remineralization played a role. When *p*CO₂ and NO₃ decreased at the beginning of August,
468 temperature simultaneously increased by 0.7 °C and salinity decreased by 0.12, suggesting that
469 entrainment of shallower water masses may have played a role too. Comprehensive analyses of
470 the factors that resulted in the 2020 differing conditions are beyond the scope of this paper, but
471 deserve attention in a future effort.

472

473 **4. Discussion**

474 CEO data provide new insights into the synoptic, seasonal and interannual variability of
475 the inorganic carbon system in a time when ocean acidification and climate change have already

476 started to transform this area. The observations suggest that the CEO site is a high- CO_2 and low-
477 pH and low- Ω_{arag} environment most of the time, except during sea ice break-up when the effects
478 of photosynthetic activity remove CO_2 from the system, and later in fall, when strong storm
479 events entrain low $p\text{CO}_2$ surface waters to the seafloor. Lowest pH and CaCO_3 saturation states
480 and highest $p\text{CO}_2$ occur in summer through late fall when organic matter remineralization
481 dominates the carbonate system balance. During this time, Ω_{arag} can fall below 0.5 and even Ω_{calc}
482 becomes sporadically undersaturated ($\Omega_{\text{calc}} < 1$).

483

484 **4.1 pH algorithm**

485 Deploying oceanographic equipment in remote Arctic locations is challenging. The data
486 return from the SeapHOx sensors was disappointingly minimal, despite annual servicing and
487 calibration by the manufacturer. Our new pH algorithm is therefore even more important as it
488 fills pH data gaps in the CEO timeseries and can be applied with confidence from the Bering to
489 the Beaufort seas (Figure 6). While another successful year of moored pH data return at the CEO
490 site is needed to fully evaluate our algorithm throughout the year, comparison with single
491 discrete water samples nearby the CEO site and the DBO dataset (section 3.1, Table 2, Figures 6
492 and S1) suggest that our algorithm-derived pH meets the weather quality uncertainty goal of \pm
493 0.02 (Newton et al., 2015) much of the time.

494 The combination of our new algorithm with recent progress in monitoring $p\text{CO}_2$ with
495 Seagliders (Hayes et al., 2022) will further increase our ability to study the inorganic carbon
496 dynamics at times and locations when shipboard or mooring based measurements may not be
497 practical. Additional assessment is needed to determine to what degree the algorithm needs
498 adjustments beyond the region evaluated in this work.

499

500 **4.2 Uncertainty**

501 Inherent spatial and temporal variability of the inorganic carbon parameters in the
502 Chukchi Sea make the use of discrete water samples for evaluating sensor-based measurements
503 difficult. Historic continuous surface measurements from the area suggest that surface $p\text{CO}_2$ can
504 be as low $< 250 \mu\text{atm}$ in early fall (Hauri et al., 2013), at a time of year when subsurface $p\text{CO}_2$
505 reaches its max of $> 800 \mu\text{atm}$ at the CEO site. This suggests a steep $p\text{CO}_2$ gradient of $> 17 \mu\text{atm}$
506 per meter. High-resolution pH data from the 2017/2018 deployment suggests high temporal
507 variability as well, further complicating the collection of discrete water samples to adequately
508 evaluate the sensors. The HydroC's zeroing function, in addition to our pre- and post-calibration
509 routines that factor into the post-processing of the data, gives us confidence in the accuracy of
510 the $p\text{CO}_2$ data, and further confidence in pH derived from $p\text{CO}_2$.

511 The pH^{est} uncertainty of 0.0525 is likely a conservative estimate based on our validation
512 of pH^{est} (section 3.1, Table 2). Consequently, propagated uncertainties in the calculated
513 parameters are high. As discussed in section 2.7, the pH- $p\text{CO}_2$ input pair exacerbates these larger
514 uncertainties. Mean $\text{TA}(\text{pH}^{\text{est}}, p\text{CO}_2)$, $\text{DIC}(\text{pH}^{\text{est}}, p\text{CO}_2)$, and $\Omega_{\text{arag}}(\text{pH}^{\text{est}}, p\text{CO}_2)$, $\pm u_c$ (Orr et al.,
515 2018) are $2173 \pm 281 \mu\text{mol kg}^{-1}$, $2111 \pm 263 \mu\text{mol kg}^{-1}$, and 0.94 ± 0.23 , respectively, when
516 input uncertainties are the standard uncertainty (Equation 1). When the input uncertainty for
517 pH^{est} is only the RMSE of 0.0161 (section 3.1), uncertainties decrease to $\pm 98 \mu\text{mol kg}^{-1}$, ± 93
518 $\mu\text{mol kg}^{-1}$, and ± 0.09 , respectively. When input uncertainties are only the random component of
519 the input parameters (i.e. standard deviation for $\text{pH}_{\text{SeaFET}}$ and $p\text{CO}_2$ and instrument precision for
520 T and S), $\text{TA}(\text{pH}_{\text{SeaFET}}, p\text{CO}_2)$, $\text{DIC}(\text{pH}_{\text{SeaFET}}, p\text{CO}_2)$, and $\Omega_{\text{arag}}(\text{pH}_{\text{SeaFET}}, p\text{CO}_2)$ u_c drops to ± 38
521 $\mu\text{mol kg}^{-1}$, $\pm 37 \mu\text{mol kg}^{-1}$, and ± 0.06 , respectively. Given the above uncertainties and that we

522 do not see significant biofouling at the CEO site, we believe that short term variability can be
523 discussed with confidence with this dataset. In other words, wiggles in the data represent real
524 events, despite the high uncertainty in the precise value of the calculated parameters.

525

526 **4.3 Subsurface biogeochemical drivers of pH, Ω_{arag} , and $p\text{CO}_2$**

527 Inorganic carbon chemistry can be influenced by advection and vertical entrainment of
528 different water masses, temperature, salinity, biogeochemistry, and conservative mixing with TA
529 and DIC freshwater endmembers. Here, we followed Rheuban et al. (2019) and separated the
530 drivers of the observed large pH, Ω_{arag} , and $p\text{CO}_2$ variability to provide additional insights into
531 our timeseries (Figure 10) using CO2SYS by altering input parameters temperature, salinity, TA,
532 and DIC. Anomalies relative to the reference values $\text{pH}(T_0, S_0, \text{DIC}_0, \text{TA}_0)$, $\Omega_{\text{arag}}(T_0, S_0, \text{DIC}_0,$
533 $\text{TA}_0)$, and $p\text{CO}_2(T_0, S_0, \text{DIC}_0, \text{TA}_0)$, were calculated using a linear Taylor series decomposition,
534 adding up the thermodynamic effects of temperature and salinity, and the perturbations due to
535 biogeochemistry, and conservative mixing with freshwater DIC and TA endmembers. (Rheuban
536 et al., 2019). Reference values T_0 , S_0 , DIC_0 , and TA_0 , are the mean of the CEO timeseries.

537 Freshwater from sea ice melt and meteoric sources (precipitation and rivers) may influence the
538 CEO site. TA and DIC concentrations of $450 \mu\text{mol kg}^{-1}$ and $400 \mu\text{mol kg}^{-1}$, respectively, have
539 been measured in Arctic sea ice (Rysgaard et al., 2007). Riverine input along the Gulf of Alaska
540 tends to have lower TA ($366 \mu\text{mol kg}^{-1}$) and DIC ($397 \mu\text{mol kg}^{-1}$) concentrations (Stackpoole et
541 al., 2016, 2017) than rivers draining into the Bering, Chukchi, and Beaufort Seas (TA = 1860
542 $\mu\text{mol kg}^{-1}$, DIC = $2010 \mu\text{mol kg}^{-1}$, Holmes et al., 2021) all of which can influence the CEO site
543 to some extent (Asahara et al., 2012; Jung et al., 2021). In this Taylor decomposition we used sea
544 ice TA and DIC endmembers (Rysgaard et al., 2007) but want to emphasize that using Arctic

545 river endmembers did not meaningfully change the results (not shown). Figure 10 shows the
546 effects of biogeochemical processes, temperature, salinity, and conservative mixing with TA and
547 DIC freshwater endmembers on pH, Ω_{arag} , and $p\text{CO}_2$. The effects of salinity (red) and
548 conservative mixing with TA and DIC freshwater endmembers (green) are negligible for pH,
549 Ω_{arag} , and $p\text{CO}_2$. Temperature varied between -1.7 °C during the sea ice covered months and up
550 to 4 °C in late fall, when wind events mixed the whole water column and entrained warm and
551 low $p\text{CO}_2$ surface waters to the instrument depth at 33 m (see section 3.2 for a more in-depth
552 discussion of these mixing events). During this time, the increase in temperature counteracted the
553 effect of biogeochemistry slightly and increased $p\text{CO}_2$ and decreased pH (Figure 10 a,c).
554 Temperature did not affect Ω_{arag} .

555 Biogeochemistry (photosynthesis, respiration, calcification, dissolution) is the most
556 important driver of the inorganic carbon dynamics at 33 m depth at the CEO site. The springtime
557 relaxation events in 2018 and 2019 with relatively higher pH and Ω_{arag} , and lower $p\text{CO}_2$, were
558 mainly driven by biogeochemistry (Figure 10). During these events O_2 increased and NO_3^-
559 decreased, suggesting photosynthetic activity (Figure 2d, e and 3a). Near bottom photosynthetic
560 activity by phytoplankton or sea ice algae has been observed at different locations across the
561 Chukchi Sea (Arrigo et al., 2017; Ouyang et al., 2022; Stabeno et al., 2020; Koch et al., 2020).
562 Sediment trap data from a CEO deployment prior to the start of this $p\text{CO}_2$ and pH time-series
563 suggest that export of the exclusively sympagic sea ice algae *Nitzschia frigida* peaked in May
564 and June, during snow and ice melt events (Lalande et al., 2020), further supporting the
565 hypothesis that sea ice algae contributed to the CO_2 draw down. Interestingly, TA also increased
566 significantly during these events in 2018 and 2019, which cannot be solely attributed to organic
567 matter production. Specifically, TA increased by 23 umol kg^{-1} in 2019 (Figure 11a). However,

568 with an observed NO_3 increase of 7.6 umol kg^{-1} , we would expect an increase of TA by 7.6 umol
569 kg^{-1} . This is assuming that NO_3 is the primary source of nitrogen during organic matter
570 formation, and that assimilation of 1 umol of NO_3 leads to an increase of TA of 1 umol (Wolf-
571 Gladrow et al., 2007). The TA increase of 23 umol kg^{-1} is therefore larger than expected from
572 organic matter formation alone and is likely due to CaCO_3 mineral dissolution. While direct
573 evidence is missing, the strong TA increase suggests that CaCO_3 mineral dissolution during sea
574 ice break up also plays an important role at the CEO site. As observed in other Arctic areas, it is
575 possible that ikaite crystals that were trapped in the ice matrix dissolved in the water column
576 when sea ice melted (Rysgaard et al., 2012, 2007).

577

578 **4.4 Progression of ocean acidification in the Chukchi Sea**

579 The Arctic Ocean acidification rate will continue to exceed the rate of CO_2 change in the
580 atmosphere because of the impacts of freshening and other more localized, seasonal or short-
581 term consequences of climate change (Woosley and Millero, 2020; Terhaar et al., 2021; Orr et
582 al., 2022; Qi et al., 2017). Seventeen years of ship-based data from sub surface Chukchi Summer
583 water suggests a mean pH change of -0.0047 ± 0.0026 and mean Ω_{arag} change of -0.017 ± 0.009
584 (Qi et al., 2022b). As a comparison, an average across historic simulations from five CMIP6
585 models (see methods) estimates a change in pH of $-0.0077 \text{ year}^{-1}$ and Ω_{arag} of $-0.0063 \text{ year}^{-1}$ at 33
586 m of the CEO site between 2002 – 2014. The historic CMIP6 simulations end in 2014 and
587 therefore miss the last years of extreme sea ice loss. Both observations and global model-based
588 trend estimates must be used with caution. The observations were collected during the sea ice
589 free period (Qi et al., 2022b), and therefore do not depict an annually representative trend.
590 Global models do not resolve important local physical, chemical, and biological meso-scale

591 processes and therefore mask out the variability of the inorganic carbon system and effects of
592 climate change.

593 Organisms living at the CEO site may have always been exposed to large seasonal
594 variability and low pH and Ω_{arag} (high $p\text{CO}_2$), but the combined and cumulative effects of
595 climate change and ocean acidification have rapidly made these conditions more extreme and
596 longer lasting. Ocean acidification serves as a gradual environmental press by increasing the
597 system's mean and extreme $p\text{CO}_2$ and decreasing mean and extreme pH and Ω_{arag} . Climate
598 induced changes to other important controls of the inorganic carbon system, such as sea ice,
599 riverine input, temperature, and circulation can act as sudden pulses and further modulate the
600 inorganic carbon system to a less predictable degree and cause extreme events (Woosley and
601 Millero, 2020; Orr et al., 2022; Hauri et al., 2021; Qi et al., 2017). Huntington et al. (2020)
602 describe a sudden and dramatic shift of the physical, biogeochemical and ecosystem conditions
603 in the Chukchi and Northern Bering seas in 2017. For example, satellite data for the CEO site
604 illustrate that the longest open water seasons on record occurred between 2017 and 2020. Before
605 2017, the open water season was on average 81 (± 40) days long (i.e., below 15 %
606 concentration), of which 60 (± 44) days were ice free, whereas between 2017 and 2020, the low
607 sea ice period was 157 (± 30) days long, of which 152 (± 24) days were ice free (Figure 12). Sea
608 ice decline and increased nutrient influx has also promoted increased phytoplankton primary
609 production in the area (Lewis et al., 2020; Arrigo and van Dijken, 2015; Payne et al., 2021).
610 Since our inorganic carbon timeseries started after the “dramatic shift” that was observed in the
611 Chukchi Sea in 2017 (Huntington et al., 2020) and given the uncertainty in model output in this
612 region, we can only speculate about how the changes in sea ice, temperature and biological
613 production may have affected seasonal variability and extremes of the inorganic carbon

614 chemistry at the CEO site. However, since the summertime low pH and Ω_{arag} and high $p\text{CO}_2$ are
615 tightly coupled to the length of the ice-free period and intensity of organic matter production, it
616 is possible that the observed summertime period of extreme conditions may have been
617 previously unexperienced at this site. We therefore think it is justified to call the spikes of pH
618 and Ω_{arag} “ocean acidification relaxation events”, since the long-lasting summertime period of
619 extremely low pH and Ω_{arag} may be a new pattern.

620

621 **4.5 Relevance for ecosystem**

622 Marine organisms are exposed to a wide range of naturally fluctuating environmental
623 conditions such as temperature, salinity, carbonate chemistry and food concentrations that
624 together constitute their ecological niche. As evolution works toward adaptation, the tolerance
625 range of species and ecosystems to such parameters varies between locations and is often closely
626 related to niche status (Vargas et al., 2022). Stress can be defined as a condition evoked in an
627 organism by one or more environmental and biological factors that bring the organism near or
628 over the limits of its ecological niche (after Van Straalen, 2003). The consequence of the
629 exposure to a stressor will depend on organismal sensitivity, stress intensity (how much it
630 deviates from present conditions) and stress duration. In a synthesis of the global literature on the
631 biological impacts of ocean acidification, Vargas et al. (2017, 2022) showed that the extreme of
632 the present range of variability of carbonate chemistry is a good predictor of species sensitivity.
633 In other words, larger deviations from present extreme high $p\text{CO}_2$ or extreme low pH, would be
634 expected to exert more negative biological impacts. Organismal stress and niche boundaries have
635 implications for the definition and understanding of controls and future ocean acidification
636 conditions in experiments aimed at evaluating future biological impacts.

637 Our data provide insights on conditions that affect and determine local species' ecological niches, and a necessary key is to evaluate or re-evaluate their sensitivity to present and future carbonate chemistry conditions, particularly for the sessile benthic calcifiers that constitute prey for mobile and upper trophic level taxa. For example, an experimental study on three common Arctic bivalve species (*Macoma calcarean*, *Astarte montagui* and *Astarte borealis*) collected in the CEO concluded that these species were generally resilient to decreasing pH (Goethel et al., 2017). However, only two pH were compared (a "control" (pH of 8.1) and an "acidified" treatment (pH of 7.8) and our results show that organisms are already experiencing more extreme conditions today than have been experimentally manipulated. While these data provide insights on these species' plasticity to present pH conditions, they cannot be used to infer sensitivity to future ocean acidification or extremes of current conditions. Based on the local adaptation hypothesis (Vargas et al. 2017, 2022), stress and associated negative effect on species fitness can be expected when pH deviates from the extreme of the present range of variability (pH<7.5) as shown in other regions (e.g. echinoderms: Dorey et al., (2013); crustaceans: Thor and Dupont, (2015); bivalves: Ventura et al., (2016)).

652 At the CEO, our results show sustained periods of remarkably low pH (e.g., 7.5; summer to fall, winter). Higher pH values are observed in spring and late fall. While we are lacking the local biological data to sufficiently evaluate past and future ecosystem changes, a high rate of ocean acidification as observed in the Chukchi Sea (Qi et al., 2022b, a), associated with potential temperature-induced shifts in the carbonate chemistry cycle (e.g. Orr et al. 2022), have the potential to impact species and ecosystems. Exposure to low pH increases organismal energy requirements for maintenance (e.g. acid-base regulation: Stumpp et al., 2012, compensatory calcification: Ventura et al., 2016). Organisms can cope with increased energy costs using a

variety of strategies, ranging from individual physiological to behavioral responses, depending on trophic level, mobility, and other ecological factors. For example, they can use available stored energy to compensate for increased costs or they can decrease their metabolism to limit costs (AMAP 2018). At the CEO, the low pH period observed during the summer and fall is associated with elevated temperature and an elevated food supply for herbivores (Lalande et al., 2020). The high availability of food may then foster compensation for the higher energetic costs associated with exposure to low pH. However, a longer period of low pH as suggested by our data could lead to a mismatch between the low pH and food availability, with cascading negative consequences for the ecosystem (Kroeker et al., 2021). In winter, the low pH conditions are associated with low temperature, no light, and low food level concentrations. These conditions are likely to keep metabolism low and limit the negative effects of exposure to low pH (Gianguzza et al., 2014). As food availability is limited by the absence of light, this strategy may be compromised by an increase in temperature that could also lead to increased metabolism. Additional work is needed to understand impacts of acidification conditions and variability on the marine biota of the Chukchi Sea, including field and laboratory experiments that evaluate biological response under realistic scenarios. The characterization of the environmental conditions at the CEO, including the variability in time, can be used to design single and multiple stressor experiments (carbonate chemistry, temperature, salinity, food, oxygen; Boyd et al. 2018).

Indigenous communities are at the forefront of the changing Arctic, including changes in accessibility, availability, and condition of traditional marine foods (Buschman and Sudlovenick, 2022; Hauser et al., 2021). Several marine species are critical to the food and cultural security of coastal Inupiat who have thrived in Arctic Alaska for millenia. While it is not possible to resolve

683 the consequences of the seasonal and interannual variations in carbonate chemistry documented
684 in this manuscript without a proper sensitivity evaluation, the seasonally low pH conditions have
685 the potential to impact organisms like bivalves in a foraging hotspot for walrus (Jay et al., 2012;
686 Kuletz et al., 2015). Walrus, as well as their bivalve stomach contents, are important nutritional,
687 spiritual, and cultural components, raising concerns for food security in the context of ecosystem
688 shifts associated with the variability and multiplicity of climate impacts within the region (ICC,
689 2015).

690

691 **5. Concluding Thoughts**

692 The Chukchi Sea is undergoing a rapid environmental transformation with potentially
693 far-reaching consequences across the ecosystem. While we are lacking a long-term time-series,
694 we used this dataset to investigate the drivers of extreme pH, Ω_{arag} , and $p\text{CO}_2$ and document
695 conditions that could affect the ecological niches of organisms, including a fast rate of ocean
696 acidification, elongated sea ice free periods, increased primary productivity and elevated
697 temperature. While a combination of experimental and monitoring approaches is needed for an
698 understanding of the ecological consequences of these changes, our results also highlight the
699 urgency to mitigate CO₂ emissions and simultaneously support Indigenous-led conservation
700 measures to safeguard an ecosystem in transition. Indigenous People in the Arctic have
701 established strategies to monitor, adapt to, and conserve the ecosystems upon which they depend.
702 Ethical and equitable engagement of Indigenous Knowledge and the communities at the forefront
703 of climate impacts can help guide research and conservation action by centering local priorities
704 and traditional practices, thereby supporting self-determination and sovereignty (Buschman and
705 Sudlovenick, 2022).

706

707 **Data availability**

708 The inorganic carbon data used in this manuscript are publicly available (Hauri and
709 Irving, 2023a; Hauri and Irving, 2023b).

710

711 **Author contributions**

712 CH and BI managed and serviced the HydroC CO₂ and SeapHOx sensors, analyzed and
713 published the data, and wrote the manuscript. SD and Peter Shipton carried out the CEO mooring
714 deployments and recoveries and managed and serviced the CTD and NO₃ sensors. RP, DH, SD,
715 and SLD contributed to the manuscript.

716

717 **Competing interests**

718 The authors have no competing interests.

719

720 **Acknowledgments**

721 The Chukchi Ecosystem Observatory is located on the traditional and contemporary
722 hunting grounds of the Northern Alaska Iñupiat. We also acknowledge that our Fairbanks-based
723 offices are located on the Native lands of the Lower Tanana Dena. The Indigenous Peoples of
724 this land never surrendered lands or resources to Russia or the United States. We acknowledge
725 this not only because we are grateful to the Indigenous communities who have been in deep
726 connection with the land and water for time immemorial, but also in recognition of the historical
727 and ongoing legacy of colonialism. We are committed to improving our scientific approaches
728 and working towards co-production for a better future for everyone.

729 We acknowledge the World Climate Research Programme, which, through its Working
730 Group on Coupled Modelling, coordinated and promoted CMIP6. We thank the climate
731 modeling groups for producing and making available their model output, the Earth System Grid
732 Federation (ESGF) for archiving the data and providing access, and the multiple funding
733 agencies who support CMIP6 and ESGF.

734

735 **Financial support**

736 We would like to thank the National Pacific Research Board Long-term Monitoring
737 (NPRB LTM) program (project no. 1426 and L-36), the Alaska Ocean Observing System (award
738 no. NA11NOS0120020 and NA16NOS0120027), and the University of Alaska Fairbanks for
739 their financial support. Claudine Hauri, Brita Irving, and Seth Danielson also acknowledge
740 support from the National Science Foundation Office of Ocean Sciences and Polar Programs
741 (OCE-1841948 and OPP-1603116). Projects that assisted in the servicing of the CEO and/or
742 collected water column calibration data were funded by the National Science Foundation, Bureau
743 of Ocean Energy Management, National Oceanic and Atmospheric Administration, National
744 Oceanographic Partnership Program, and Shell Exploration and Production Company, Inc.
745 Maintenance and calibration of the CEO sensors is only possible due to the kind support of
746 numerous collaborators within the Arctic research community who helped with CEO deployment
747 and recovery or collected sensor calibration samples. We would therefore like to thank Peter
748 Shipton, Carin Ashjian, Jessica Cross, Miguel Goñi, Jackie Grebmeier, Burke Hales, Katrin Iken,
749 Laurie Juranek, Calvin Mordy, and Robert Pickart.

750

751 **References**

752 Alin, S. R., Feely, R. A., Dickson, A. G., Hernández-Ayón, J. M., Juranek, L. W., Ohman, M.
753 D., and Goericke, R.: Robust empirical relationships for estimating the carbonate system in the
754 southern California Current System and application to CalCOFI hydrographic cruise data (2005–
755 2011), *Journal of Geophysical Research*, 117, C05033, doi:10.1029/2011JC007511, 2012.

756

757 AMAP. AMAP Assessment 2018: Arctic Ocean Acidification. Arctic Monitoring and
758 Assessment Programme (AMAP), Tromsø, Norway. vi+187pp,
759 [https://www.apmap.no/documents/doc/AMAP-Assessment-2018-Arctic-Ocean-](https://www.apmap.no/documents/doc/AMAP-Assessment-2018-Arctic-Ocean-Acidification/1659)
760 Acidification/1659, 2018.

761

762 Arrigo, K. R. and van Dijken, G. L.: Continued increases in Arctic Ocean primary production,
763 *Prog. Oceanogr.*, 136, 60–70, <https://doi.org/10.1016/j.pocean.2015.05.002>, 2015.

764

765 Asahara, Y., Takeuchi, F., Nagashima, K., Harada, N., Yamamoto, K., Oguri, K., and Tada, O.:
766 Provenance of terrigenous detritus of the surface sediments in the Bering and Chukchi Seas as
767 derived from Sr and Nd isotopes: Implications for recent climate change in the Arctic regions,
768 *Deep Sea Res. Part II Top. Stud. Oceanogr.*, 61–64, 155–171,
769 <https://doi.org/10.1016/j.dsr2.2011.12.004>, 2012.

770

771 Bates, N. R., Mathis, J. T. and Cooper, L. W.: Ocean acidification and biologically induced
772 seasonality of carbonate mineral saturation states in the western Arctic Ocean. *J. Geophys. Res.*
773 114, 2008JC004862, 2009.

774

775 Bednaršek, N., Calosi, P., Feely, R. A., Ambrose, R., Byrne, M., Chan, K. Y. K., Dupont, S.,
776 Padilla-Gamiño, J. L., Spicer, J. I., Kessouri, F., Roethler, M., Sutula, M., and Weisberg, S. B.:
777 Synthesis of thresholds of ocean acidification impacts on echinoderms, *Front. Mar. Sci.*,
778 8, <https://doi.org/10.3389/fmars.2021.602601>, 2021.

779

780 Bittig, H. C., Steinhoff, T., Claustre, H., Fiedler, B., Williams, N. L., Sauzède, R., Körtzinger,
781 A., and Gattuso, J.-P.: An alternative to static climatologies: robust estimation of open ocean
782 CO₂ variables and nutrient concentrations from T, S, and O₂ data using Bayesian neural
783 networks, *Front. Mar. Sci.*, 5, 328, <https://doi.org/10.3389/fmars.2018.00328>, 2018.

784

785 Blanchard, A. L., Parris, C. L., Knowlton, A. L. and Wade, N. R.: Benthic ecology of the
786 northeastern Chukchi Sea. Part I. Environmental characteristics and macrofaunal community
787 structure, 2008–2010. *Continental Shelf Research* 67, 52–66, 2013.

788

789 Boucher, O., Denvil, S., Levavasseur, G., Cozic, A., Caubel, A., Foujols, M.-A., Meurdesoif, Y.,
790 Balkanski, Y., Checa-Garcia, R., Hauglustaine, D., Bekki, S. and Marchand, M.: IPSL IPSL-
791 CM6A-LR-INCA model output prepared for CMIP6 AerChemMIP.
792 doi:10.22033/ESGF/CMIP6.13581, 2020.

793

794 Boyd, P. W., Collins, S., Dupont, S., Fabricius, K., Gattuso, J.-P., Havenhand, J., Hutchins, D.
795 A., Riebesell, U., Rintoul, M. S., Vichi, M., Biswas, H., Ciotti, A., Gao, K., Gehlen, M., Hurd, C.
796 L., Kurihara, H., McGraw, C. M., Navarro, J. M., Nilsson, G. E., Passow, U. and Pörtner, H.-O.:

797 Experimental strategies to assess the biological ramifications of multiple drivers of global ocean
798 change—A review. *Global Change Biology* 24, 2239–2261, 2018.

799

800 Breitberg, D., Salisbury, J., Bernhard, J., Cai, W.-J., Dupont, S., Doney, S., Kroeker,
801 K., Levin, L.A., Long, W. C., Milke, L.M., Miller S.H., Phelan, B., Passow, U., Seibel,
802 B.A., Todgham, A.E., and Tarrant, A.M.: And on top of all that... Coping with ocean
803 acidification in the midst of many stressors. *Oceanography*, 25(2), 48–61.
804 <https://doi.org/10.5670/oceanog.2015.31>, 2015.

805

806 Bresnahan, P. J., Martz, T. R., Takeshita, Y., Johnson, K. S., and LaShomb, M.: Best practices
807 for autonomous measurement of seawater pH with the Honeywell Durafet, *Methods Oceanogr.*,
808 9, 44–60, <https://doi.org/10.1016/j.mio.2014.08.003>, 2014.

809

810 Brodzik, M. J. and K. W. Knowles: “Chapter 5: EASE-Grid: A Versatile Set of Equal-Area
811 Projections and Grids.” in Michael F. Goodchild (Ed.) *Discrete Global Grids: A Web Book*.
812 Santa Barbara, California USA: National Center for Geographic Information & Analysis.
813 <https://escholarship.org/uc/item/9492q6sm>, 2002.

814

815 Buschman, V. Q. and Sudlovenick, E.: Indigenous-led conservation in the Arctic supports global
816 conservation practices, *Arctic Science*, 9(3): 714-719, <https://doi.org/10.1139/as-2022-0025>,
817 2022.

818

819 Carmack, E. and Wassmann, P.: Food webs and physical–biological coupling on pan-Arctic
820 shelves: unifying concepts and comprehensive perspectives. *Progress in Oceanography*, 71(2-4),
821 pp.446-477, 2006.

822

823 Carter, B. R., Feely, R. A., Williams, N. L., Dickson, A. G., Fong, M. B., and Takeshita, Y.:
824 Updated methods for global locally interpolated estimation of alkalinity, pH, and nitrate,
825 *Methods Limnology and Oceanography*, 16(2), 119-131, <https://doi.org/10.1002/lom3.10232>,
826 2018.

827

828 Chatterjee, S., and Hadi, A. S.: “Influential Observations, High Leverage Points, and Outliers in
829 Linear Regression.” *Statistical Science*, 1(3), 1986, pp. 379–416, 10.1214/ss/1177013622, 1986.

830

831 Corlett, W. B. and Pickart, R. S.: The Chukchi slope current. *Progress in Oceanography* 153, 50–
832 65, 2017.

833

834 Cross, J. N., Mathis, J. T., Bates, N. R., and Byrne, R. H.: Conservative and non-conservative
835 variations of total alkalinity on the Southeastern Bering Sea Shelf, *Mar. Chem.*, 154, 100–112,
836 <https://doi.org/10.1016/j.marchem.2013.05.012>, 2013.

837

838 Cross, J. N., Monacci, N. M., Bell, S. W., Grebmeier, J. M., Mordy, C., Pickart, R. S., Stabeno,
839 and P. J.: Dissolved inorganic carbon (DIC), total alkalinity (TA) and other variables collected
840 from discrete samples and profile observations from United States Coast Guard Cutter (USCGC)
841 Healy cruise HLY1702 (EXPOCODE 33HQ20170826) in the Bering and Chukchi Sea along

842 transect lines in the Distributed Biological Observatory (DBO) from 2017-08-26 to 2017-09-15
843 (NCEI Accession 0208337). NOAA National Centers for Environmental Information. Dataset.
844 <https://doi.org/10.25921/pks4-4p43>, 2020a.

845

846 Cross, J. N., Monacci, N. M., Bell, S. W., Grebmeier, J. M., Mordy, C., Pickart, R. S., and
847 Stabeno, P. J.: Dissolved inorganic carbon (DIC), total alkalinity (TA) and other parameters
848 collected from discrete sample and profile observations during the USCGC Healy cruise
849 HLY1801 (EXPOCODE 33HQ20180807) in the Bering Sea, Chukchi Sea and Beaufort Sea
850 along transect lines in the Distributed Biological Observatory (DBO) from 2018-08-07 to 2018-
851 08-24 (NCEI Accession 0221911). NOAA National Centers for Environmental Information.
852 Dataset. <https://doi.org/10.25921/xc4b-xh20>, 2020b.

853

854 Cross, J. N., Monacci, N. M., Bell, S. W., Grebmeier, J. M., Mordy, C., Pickart, Robert S.,
855 Stabeno, P.J.: Dissolved inorganic carbon (DIC) and total alkalinity (TA) and other hydrographic
856 and chemical data collected from discrete sample and profile observations during the United
857 States Coast Guard Cutter (USCGC) Healy cruise HLY1901 (EXPOCODE 33HQ20190806) in
858 the Bering and Chukchi Sea along transect lines in the Distributed Biological Observatory
859 (DBO) from 2019-08-06 to 2019-08-22 (NCEI Accession 0243277). NOAA National Centers for
860 Environmental Information. Dataset. <https://doi.org/10.25921/b5s5-py61>, 2021.

861

862 Cullison-Gray, S. E., DeGrandpre, M. D., Moore, T. S., Martz, T. R., Friederich, G. E., and
863 Johnson, K. S.: Applications of in situ pH measurements for inorganic carbon calculations, Mar.
864 Chem., 125, 82–90, <https://doi.org/10.1016/j.marchem.2011.02.005>, 2011.

865

866 Daniel, A., Laës-Huon, A., Barus, C., Beaton, A. D., Blandfort, D., Guigues, N., Knockaert, M.,
867 Munaron, D., Salter, I., Woodward, E. M. S., Greenwood, N., and Achterberg, E. P.: Toward a
868 harmonization for using in situ nutrient sensors in the marine environment, *Front. Mar. Sci.*, 6,
869 773, <https://doi.org/10.3389/fmars.2019.00773>, 2020.

870

871 Danielson, S.L., Iken, K., Hauri, C., Hopcroft, R.R., McDonnell, A.M., Winsor, P., Lalande, C.,
872 Grebmeier, J.M., Cooper, L.W., Horne, J.K. and Stafford, K.M.: Collaborative approaches to
873 multi-disciplinary monitoring of the Chukchi shelf marine ecosystem: Networks of networks for
874 maintaining long-term Arctic observations. In *OCEANS 2017-Anchorage* (pp. 1-7). IEEE, 2017.

875

876 Danielson, S. L., Ahkinga, O., Ashjian, C., Basyuk, E., Cooper, L. W., Eisner, L., Farley, E.,
877 Iken, K. B., Grebmeier, J. M., Juranek, L., Khen, G., Jayne, S. R., Kikuchi, T., Ladd, C., Lu, K.,
878 McCabe, R. M., Moore, G. W. K., Nishino, S., Ozenna, F., Pickart, R. S., Polyakov, I., Stabeno,
879 P. J., Thoman, R., Williams, W. J., Wood, K., and Weingartner, T. J.: Manifestation and
880 consequences of warming and altered heat fluxes over the Bering and Chukchi Sea continental
881 shelves, *Deep Sea Res. Part II Top. Stud. Oceanogr.*, 177, 104781,
882 <https://doi.org/10.1016/j.dsr2.2020.104781>, 2020.

883

884 Danielson, S.: Water temperature, conductivity, and others taken by CTD and Niskin bottles
885 from the research vessel Norseman II Data for Arctic Marine Biodiversity Observing Network,
886 AMBON, Program in the Chukchi Sea from 2017-08-07 to 2017-08-22 (NCEI Accession

887 0229072). NOAA National Centers for Environmental Information. Dataset.
888 <https://doi.org/10.25921/afz7-0d98>, 2021.

889

890 DeGrandpre, M. D., Lai, C.-Z., Timmermans, M.-L., Krishfield, R. A., Proshutinsky, A. and
891 Torres, D.: Inorganic Carbon and pCO₂ Variability During Ice Formation in the Beaufort Gyre of
892 the Canada Basin. *Journal of Geophysical Research: Oceans* 124, 4017–4028, 2019.

893

894 Dickson, A. G.: Thermodynamics of the dissociation of boric acid in synthetic seawater from
895 273.15 to 318.15 K, *Deep Sea Res. Part Oceanogr. Res. Pap.*, 37, 755–766,
896 [https://doi.org/10.1016/0198-0149\(90\)90004-F](https://doi.org/10.1016/0198-0149(90)90004-F), 1990.

897

898 Dickson, A. G., Sabine, C. L., and Christian, J. R.: Guide to best practices for ocean CO₂
899 measurements, PICES, Sydney, 191 pp., 2007.

900

901 DiGirolamo, N. E., C. L. Parkinson, D. J. Cavalieri, P. Gloersen, and H. J. Zwally: Sea Ice
902 Concentrations from Nimbus-7 SMMR and DMSP SSM/I-SSMIS Passive Microwave Data,
903 Version 2. Boulder, Colorado USA. NASA National Snow and Ice Data Center Distributed
904 Active Archive Center. <https://doi.org/10.5067/MPYG15WAA4WX>, 2022.

905

906 Dorey, N., Lançon, P., Thorndyke, M., and Dupont, S.: Assessing physiological tipping point of
907 sea urchin larvae exposed to a broad range of pH, *Glob. Change Biol.*, 19, 3355–3367,
908 <https://doi.org/10.1111/gcb.12276>, 2013.

909

910 Doney, S. C., Busch, D. S., Cooley, S. R. and Kroeker, K. J.: The Impacts of Ocean
911 Acidification on Marine Ecosystems and Reliant Human Communities. *Annu. Rev. Environ.*
912 *Resour.* 45, 83–112, 2020.

913

914 Duke, P. J., Else, B. G. T., Jones, S. F., Marriot, S., Ahmed, M. M. M., Nandan, V., Butterworth,
915 B., Gonski, S. F., Dewey, R., Sastri, A., Miller, L. A., Simpson, K. G., and Thomas, H.: Seasonal
916 marine carbon system processes in an Arctic coastal landfast sea ice environment observed with
917 an innovative underwater sensor platform, *Elementa: Science of the Anthropocene*, 9 (1): 00103,
918 <https://doi.org/10.1525/elementa.2021.00103>, 2021.

919

920 Etminan, M., Myhre, G., Highwood, E. J., and Shine, K. P.: Radiative forcing of carbon dioxide,
921 methane, and nitrous oxide: A significant revision of the methane radiative forcing, *Geophys.*
922 *Res. Lett.*, 43, 12,614-12,623, <https://doi.org/10.1002/2016GL071930>, 2016.

923

924 Fang, Y.C., Weingartner, T.J., Dobbins, E.L., Winsor, P., Statscewich, H., Potter, R.A., Mudge,
925 T.D., Stoudt, C.A. and Borg, K.: Circulation and thermohaline variability of the Hanna Shoal
926 region on the northeastern Chukchi Sea shelf. *Journal of Geophysical Research: Oceans*, 125(7),
927 p.e2019JC015639, 2020.

928

929 Fietzek, P., Fiedler, B., Steinhoff, T., and Körtzinger, A.: In situ quality assessment of a novel
930 underwater CO₂ sensor based on membrane equilibration and NDIR spectrometry, *J.*
931 *Atmospheric Ocean. Technol.*, 31, 181–196, <https://doi.org/10.1175/JTECH-D-13-00083.1>,
932 2014.

933

934 Friis, K.: The salinity normalization of marine inorganic carbon chemistry data, *Geophys. Res.*
935 Lett.

936

937 Gianguzza, P., Visconti, G., Gianguzza, F., Vizzini, S., Sarà, G., and Dupont, S.: Temperature
938 modulates the response of the thermophilous sea urchin *Arbacia lixula* early life stages to CO₂-
939 driven acidification, *Mar. Environ. Res.*, 93, 70–77,
940 <https://doi.org/10.1016/j.marenvres.2013.07.008>, 2014.

941

942 Goethel, C. L., Grebmeier, J. M., Cooper, L. W., and Miller, T. J.: Implications of ocean
943 acidification in the Pacific Arctic: Experimental responses of three Arctic bivalves to decreased
944 pH and food availability, *Deep Sea Res. Part II Top. Stud. Oceanogr.*, 144, 112–124,
945 <https://doi.org/10.1016/j.dsr2.2017.08.013>, 2017.

946

947 Gonzalez, S., Horne, J. K., and Danielson, S. L.: Multi-scale temporal variability in biological-
948 physical associations in the NE Chukchi Sea, *Polar Biol.*, 44, 837–855,
949 <https://doi.org/10.1007/s00300-021-02844-1>, 2021.

950

951 Grebmeier, J. M., Bluhm, B. A., Cooper, L. W., Danielson, S. L., Arrigo, K. R., Blanchard, A.
952 L., Clarke, J. T., Day, R. H., Frey, K. E., Gradinger, R. R., Kędra, M., Konar, B., Kuletz, K. J.,
953 Lee, S. H., Lovvorn, J. R., Norcross, B. L. and Okkonen, S. R.: Ecosystem characteristics and
954 processes facilitating persistent macrobenthic biomass hotspots and associated benthivory in the

955 Pacific Arctic. *Progress in Oceanography* 136, 92–114,

956 <https://doi.org/10.1016/j.pocean.2015.05.006>, 2015.

957

958 Hauri, C., Gruber, N., Vogt, M., Doney, S. C., Feely, R. A., Lachkar, Z., Leinweber, A.,

959 McDonnell, A. M. P., Munnich, M. and Plattner, G.-K.: Spatiotemporal variability and long-term

960 trends of ocean acidification in the California Current System. *Biogeosciences* 10, 193–216,

961 <https://doi.org/10.5194/bg-10-193-2013>, 2013.

962

963 Hauri, C., Danielson, S., McDonnell, A. M. P., Hopcroft, R. R., Winsor, P., Shipton, P., Lalande,

964 C., Stafford, K. M., Horne, J. K., Cooper, L. W., Grebmeier, J. M., Mahoney, A., Maisch, K.,

965 McCammon, M., Statscewich, H., Sybrandy, A., and Weingartner, T.: From sea ice to seals: a

966 moored marine ecosystem observatory in the Arctic, *Ocean Sci.*, 14, 1423–1433,

967 <https://doi.org/10.5194/os-14-1423-2018>, 2018.

968

969 Hauri, C., Pagès, R., McDonnell, A. M. P., Stuecker, M. F., Danielson, S. L., Hedstrom, K.,

970 Irving, B., Schultz, C., and Doney, S. C.: Modulation of ocean acidification by decadal climate

971 variability in the Gulf of Alaska, *Communications Earth & Environment* 2, 191,

972 <https://doi.org/10.1038/s43247-021-00254-z>, 2021.

973

974 Hauri, C. and Irving, B.: pCO₂ time series measurements from the Chukchi Ecosystem

975 Observatory CEO2 mooring deployed at 33 meters depth in the Northeast Chukchi Sea. *Research*

976 *Workspace*. <https://doi.org/10.24431/rw1k7dq>.

977 version: 10.24431_rw1k7dq_20230531T123002Z, 2023a.

978

979 Hauri, C. and Irving, B.: pH, temperature, salinity, and oxygen time series measurements from
980 the Chukchi Ecosystem Observatory CEO2 mooring deployed at 33 meters depth in the
981 Northeast Chukchi Sea. Research Workspace. <https://doi.org/10.24431/rw1k7dp>,
982 version: 10.24431_rw1k7dp_20230531T121136Z, 2023b.

983

984 Hauser, D. D. W., Whiting, A. V., Mahoney, A. R., Goodwin, J., Harris, C., Schaeffer, R. J.,
985 Schaeffer, R., Laxague, N. J. M., Subramaniam, A., Witte, C. R., Betcher, S., Lindsay, J. M., and
986 Zappa, C. J.: Co-production of knowledge reveals loss of Indigenous hunting opportunities in the
987 face of accelerating Arctic climate change, *Environ. Res. Lett.*, 16, 095003,
988 <https://doi.org/10.1088/1748-9326/ac1a36>, 2021.

989

990 Hayes, D., Kemme, J., and Hauri C.: Ocean greenhouse gas monitoring: new autonomous
991 platform to measure pCO₂, methane, *Sea Technology*, 63(10), 13-16, [https://lsc-
992 pagepro.mydigitalpublication.com/publication/?i=764237&p=13&view=issueViewer](https://lsc-pagepro.mydigitalpublication.com/publication/?i=764237&p=13&view=issueViewer), 2022.

993

994 Hennon, T. D., Danielson, S. L., Woodgate, R. A., Irving, B., Stockwell, D. A., and Mordy, C.
995 W.: Mooring Measurements of Anadyr Current Nitrate, Phosphate, and Silicate Enable Updated
996 Bering Strait Nutrient Flux Estimates, *Geophys. Res. Lett.*, 49, e2022GL098908,
997 <https://doi.org/10.1029/2022GL098908>, 2022.

998

999 Holmes, R.M., J.W. McClelland, S.E. Tank, R.G.M. Spencer, and A.I. Shiklomanov.: Arctic
1000 Great Rivers Observatory. Water Quality Dataset, <https://www.arcticgreatrivers.org/data>, 2021.

1001

1002 Horowitz, L. W., Naik, V., Sentman, L., Paulot, F., Blanton, C., McHugh, C., Radhakrishnan, A.,

1003 Rand, K., Vahlenkamp, H., Zadeh, N. T., Wilson, C., Ginoux, P., He, J., John, J. G., Lin, M.,

1004 Paynter, D. J., Ploshay, J., Zhang, A. and Zeng, Y.: NOAA-GFDL GFDL-ESM4 model output

1005 prepared for CMIP6 AerChemMIP hist-1950HC. doi:10.22033/ESGF/CMIP6.8568, 2018.

1006

1007 Huntington, H. P., Danielson, S. L., Wiese, F. K., Baker, M., Boveng, P., Citta, J. J., De

1008 Robertis, A., Dickson, D. M. S., Farley, E., George, J. C., Iken, K., Kimmel, D. G., Kuletz, K.,

1009 Ladd, C., Levine, R., Quakenbush, L., Stabeno, P., Stafford, K. M., Stockwell, D., and Wilson,

1010 C.: Evidence suggests potential transformation of the Pacific Arctic ecosystem is underway, *Nat.*

1011 *Clim. Change*, 10, 342–348, <https://doi.org/10.1038/s41558-020-0695-2>, 2020.

1012

1013 Huntington, H. P., Zagorsky, A., Kaltenborn, B. P., Shin, H. C., Dawson, J., Lukin, M., Dahl, P.

1014 E., Guo, P., and Thomas, D. N.: Societal implications of a changing Arctic Ocean. *Ambio*, 51(2),

1015 298–306. <https://doi.org/10.1007/s13280-021-01601-2>, 2022.

1016

1017 ICC: Alaskan Inuit food security conceptual framework: how to assess the Arctic from an Inuit

1018 perspective, Inuit Circumpolar Council-Alaska, Anchorage, 2015.

1019

1020 Irving, B., SUNA_V2_processing, GitHub repository, https://github.com/britairving/SUNA_V2,

1021 2021.

1022

1023 Islam, F., DeGrandpre, M. D., Beatty, C.M., Timmermanns, M.-L., Krishfield, R. A., Toole,
1024 J.M., and Laney, S.R.: Sea surface pCO₂ and O₂ dynamics in the partially ice-covered Arctic
1025 Ocean, *JGR Oceans*, 122(2), 1425-1438, <https://doi.org/10.1002/2016JC012162>, 2016.

1026

1027 Jay, C. V., Fischbach, A. S., and Kochnev, A. A.: Walrus areas of use in the Chukchi Sea during
1028 sparse sea ice cover, *Mar. Ecol. Prog. Ser.*, 468, 1–13, <https://doi.org/10.3354/meps10057>, 2012.

1029

1030 Jiang, L.-Q., Feely, R. A., Wanninkhof, R., Greeley, D., Barbero, L., Alin, S., Carter, B. R.,
1031 Pierrot, D., Featherstone, C., Hooper, J., Melrose, C., Monacci, N., Sharp, J. D., Shellito, S., Xu,
1032 Y.-Y., Kozyr, A., Byrne, R. H., Cai, W.-J., Cross, J., Johnson, G. C., Hales, B., Langdon, C.,
1033 Mathis, J., Salisbury, J., and Townsend, D. W.: Coastal Ocean Data Analysis Product in North
1034 America (CODAP-NA) – an internally consistent data product for discrete inorganic carbon,
1035 oxygen, and nutrients on the North American ocean margins, *Earth Syst. Sci. Data*, 13, 2777–
1036 2799, <https://doi.org/10.5194/essd-13-2777-2021>, 2021.

1037

1038 Jung, J., Son, J. E., Lee, Y. K., Cho, K.-H., Lee, Y., Yang, E. J., Kang, S.-H., and Hur, J.:
1039 Tracing riverine dissolved organic carbon and its transport to the halocline layer in the Chukchi
1040 Sea (western Arctic Ocean) using humic-like fluorescence fingerprinting, *Sci. Total Environ.*,
1041 772, 145542, <https://doi.org/10.1016/j.scitotenv.2021.145542>, 2021.

1042

1043 Juranek, L. W., Feely, R. A., Peterson, W. T., Alin, S. R., Hales, B., Lee, K., Sabine, C. L., and
1044 Peterson, J.: A novel method for determination of aragonite saturation state on the continental

1045 shelf of central Oregon using multi-parameter relationships with hydrographic data, *Geophys.*
1046 *Res. Lett.*, 36, L24601, <https://doi.org/10.1029/2009GL040778>, 2009.

1047

1048 Juranek, L. W., Feely, R. A., Gilbert, D., Freeland, H., and Miller, L. A.: Real-time estimation of
1049 pH and aragonite saturation state from Argo profiling floats: Prospects for an autonomous carbon
1050 observing strategy, *Geophys. Res. Lett.*, 38, L17603, <https://doi.org/10.1029/2011gl048580>,
1051 2011.

1052

1053 Koch, C. W., Cooper, L. W., Lalande, C., Brown, T. A., Frey, K. E. and Grebmeier, J. M.:
1054 Seasonal and latitudinal variations in sea ice algae deposition in the Northern Bering and
1055 Chukchi Seas determined by algal biomarkers. *PLoS ONE* 15, e0231178, 2020.

1056

1057 Kroeker, K. J., Powell, C., and Donham, E. M.: Windows of vulnerability: Seasonal mismatches
1058 in exposure and resource identity determine ocean acidification's effect on a primary consumer
1059 at high latitude, *Glob. Change Biol.*, 27, 1042–1051, <https://doi.org/10.1111/gcb.15449>, 2021.

1060

1061 Kuletz, K. J., Ferguson, M. C., Hurley, B., Gall, A. E., Labunski, E. A., and Morgan, T. C.:
1062 Seasonal spatial patterns in seabird and marine mammal distribution in the eastern Chukchi and
1063 western Beaufort seas: Identifying biologically important pelagic areas, *Prog. Oceanogr.*, 136,
1064 175–200, <https://doi.org/10.1016/j.pocean.2015.05.012>, 2015.

1065

1066 Lalande, C., Grebmeier, J. M., Hopcroft, R. R., and Danielson, S. L.: Annual cycle of export
1067 fluxes of biogenic matter near Hanna Shoal in the northeast Chukchi Sea, Deep Sea Res. Part II
1068 Top. Stud. Oceanogr., 177, 104730, <https://doi.org/10.1016/j.dsr2.2020.104730>, 2020.

1069

1070 Lalande, C., Grebmeier, J. M., McDonnell, A. M. P., Hopcroft, R. R., O'Daly, S., and Danielson,
1071 S. L.: Impact of a warm anomaly in the Pacific Arctic region derived from time-series export
1072 fluxes, PLOS ONE, 16, e0255837, <https://doi.org/10.1371/journal.pone.0255837>, 2021.

1073

1074 Lauvset, S. K., Lange, N., Tanhua, T., Bittig, H. C., Olsen, A., Kozyr, A., Álvarez, M., Becker,
1075 S., Brown, P. J., Carter, B. R., Cotrim da Cunha, L., Feely, R. A., van Heuven, S., Hoppema, M.,
1076 Ishii, M., Jeansson, E., Jutterström, S., Jones, S. D., Karlsen, M. K., Lo Monaco, C., Michaelis,
1077 P., Murata, A., Pérez, F. F., Pfeil, B., Schirnick, C., Steinfeldt, R., Suzuki, T., Tilbrook, B., Velo,
1078 A., Wanninkhof, R., Woosley, R. J., and Key, R. M.: An updated version of the global interior
1079 ocean biogeochemical data product, GLODAPv2.2021, Earth Syst. Sci. Data Discuss.,
1080 <https://doi.org/10.5194/essd-2021-234>, 2021.

1081

1082 Laws, E. A.: Photosynthetic quotients, new production and net community production in the
1083 open ocean, Deep Sea Res. Part Oceanogr. Res. Pap., 38, 143–167, [https://doi.org/10.1016/0198-0149\(91\)90059-O](https://doi.org/10.1016/0198-0149(91)90059-O), 1991.

1085

1086 Lee, K., Kim, T.-W., Byrne, R. H., Millero, F. J., Feely, R. A., and Liu, Y.-M.: The universal
1087 ratio of boron to chlorinity for the North Pacific and North Atlantic oceans, Geochim.
1088 Cosmochim. Acta, 74, 1801–1811, <https://doi.org/10.1016/j.gca.2009.12.027>, 2010.

1089

1090 Lewis, E. and Wallace, D. W. R.: Program Developed for CO₂ System Calculations,
1091 ORNL/CDIAC-105, Carbon Dioxide Inf. Anal. Cent., Oak Ridge Natl. Lab., Oak Ridge, Tenn.,
1092 38 pp., <https://salish-sea.pnnl.gov/media/ORNL-CDIAC-105.pdf>, 1998.

1093

1094 Lewis, K. M., van Dijken, G. L., and Arrigo, K. R.: Changes in phytoplankton concentration now
1095 drive increased Arctic Ocean primary production, *Science*, 369, 198–202,
1096 <https://doi.org/10.1126/science.aay8380>, 2020.

1097

1098 Li, B., Watanabe, Y. W., and Yamaguchi, A.: Spatiotemporal distribution of seawater pH in the
1099 North Pacific subpolar region by using the parameterization technique, *J. Geophys. Res. Oceans*,
1100 121, 3435–3449, <https://doi.org/10.1002/2015JC011615>, 2016.

1101

1102 Licker, R., Ekwurzel, B., Doney, S. C., Cooley, S. R., Lima, I. D., Heede, R., and Frumhoff, P.
1103 C.: Attributing ocean acidification to major carbon producers, *Environ. Res. Lett.*, 14, 124060,
1104 <https://doi.org/10.1088/1748-9326/ab5abc>, 2019.

1105

1106 Lueker, T. J., Dickson, A. G., and Keeling, C. D.: Ocean pCO₂ calculated from dissolved
1107 inorganic carbon, alkalinity, and equations for K 1 and K 2: validation based on laboratory
1108 measurements of CO₂ in gas and seawater at equilibrium, *Mar. Chem.*, 70, 105–119,
1109 [https://doi.org/10.1016/S0304-4203\(00\)00022-0](https://doi.org/10.1016/S0304-4203(00)00022-0), 2000.

1110

1111 Mathis, J. T. and Questel, J. M.: Assessing seasonal changes in carbonate parameters across
1112 small spatial gradients in the Northeastern Chukchi Sea. *Continental Shelf Research* 67, 42–51,
1113 <https://doi.org/10.1016/j.csr.2013.04.041>, 2013.

1114

1115 Martz, T. R., Connery, J. G., and Johnson, K. S.: Testing the Honeywell Durafet for seawater pH
1116 applications, *Limnol. Oceanogr. Methods*, 8, 172–184, <https://doi.org/10.4319/lom.2010.8.172>,
1117 2010.

1118

1119 Mauritsen, T., Bader, J., Becker, T., Behrens, J., Bittner, M., Brokopf, R., Brovkin, V., Claussen,
1120 M., Crueger, T., Esch, M., Fast, I., Fiedler, S., Fläschner, D., Gayler, V., Giorgetta, M., Goll, D.
1121 S., Haak, H., Hagemann, S., Hedemann, C., Hohenegger, C., Ilyina, T., Jahns, T., Jiménez-de-la-
1122 Cuesta, D., Jungclaus, J., Kleinen, T., Kloster, S., Kracher, D., Kinne, S., Kleberg, D., Lasslop,
1123 G., Kornblueh, L., Marotzke, J., Matei, D., Meraner, K., Mikolajewicz, U., Modali, K., Möbis,
1124 B., Müller, W. A., Nabel, J. E. M. S., Nam, C. C. W., Notz, D., Nyawira, S.-S., Paulsen, H.,
1125 Peters, K., Pincus, R., Pohlmann, H., Pongratz, J., Popp, M., Raddatz, T. J., Rast, S., Redler, R.,
1126 Reick, C. H., Rohrschneider, T., Schemann, V., Schmidt, H., Schnur, R., Schulzweida, U., Six,
1127 K. D., Stein, L., Stemmler, I., Stevens, B., von Storch, J.-S., Tian, F., Voigt, A., Vreese, P.,
1128 Wieners, K.-H., Wilkenskjeld, S., Winkler, A., and Roeckner, E.: Developments in the MPI-M
1129 Earth System Model version 1.2 (MPI-ESM1.2) and Its Response to Increasing CO₂, *J. Adv.*
1130 *Model. Earth Syst.*, 11, 998–1038, <https://doi.org/10.1029/2018MS001400>, 2019.

1131

1132 McDougall, T.J. and Barker, P.M.: Getting started with TEOS-10 and the Gibbs Seawater
1133 (GSW) Oceanographic Toolbox, 28pp., SCOR/IAPSO WG127, ISBN 978-0-646-55621-5, 2011.

1134

1135 McRaven, L. and Pickart, R.: Conductivity-Temperature-Depth (CTD) data from the 2018
1136 Distributed Biological Observatory - Northern Chukchi Integrated Study (DBO-NCIS) cruise on
1137 USCGC (US Coast Guard Cutter) Healy (HLY1801). Arctic Data Center.
1138 doi:10.18739/A2HT2GC7Z, 2021.

1139

1140 Monacci, N. M., Cross, J. N., Pickart, R. S., Juranek, L. W., McRaven, L. T., and Becker, S.:
1141 Dissolved inorganic carbon (DIC) and total alkalinity (TA) and other hydrographic and chemical
1142 data collected from discrete sample and profile observations aboard the RV Sikuliaq Cruise
1143 SKQ202014S (EXPOCODE 33BI20201025) in the Bering and Chukchi Sea along transect lines
1144 in the Distributed Biological Observatory (DBO) from 2020-10-25 to 2020-11-11 (NCEI
1145 Accession 0252613). NOAA National Centers for Environmental Information. Dataset.
1146 <https://doi.org/10.25921/pnsd-sv10>, 2022.

1147

1148 Moore, S. E., Douglas P. deMaster, and Paul K. Dayton: Cetacean Habitat Selection in the
1149 Alaskan Arctic during Summer and Autumn, *Arctic*, 53(4), 432–47. JSTOR,
1150 <http://www.jstor.org/stable/40512256>, 2000.

1151

1152 Moore, S. E., and Stabeno, P. J.: Synthesis of Arctic Research (SOAR) in marine ecosystems of
1153 the Pacific Arctic, *Progress in Oceanography*, 136, 1-11,
1154 <https://doi.org/10.1016/j.pocean.2015.05.017>, 2015,

1155

1156 Moore, S. E., Clarke, J. T., Okkonen, S. R., Grebmeier, J. M., Berchok, C. L., and Stafford, K.
1157 M.: Changes in gray whale phenology and distribution related to prey variability and ocean
1158 biophysics in the northern Bering and eastern Chukchi seas. PLOS ONE 17(4):
1159 e0265934. <https://doi.org/10.1371/journal.pone.0265934>, 2022.
1160
1161 Moore, G., Steele, M., Schweiger, A.J. et al.: Thick and old sea ice in the Beaufort Sea during
1162 summer 2020/21 was associated with enhanced transport: Commun Earth Environ3, 198
1163 <https://doi.org/10.1038/s43247-022-00530-6>, 2022.
1164
1165 Mordy, C. W., Bell, S., Cokelet, E. D., Ladd, C., Lebon, G., Proctor, P., Stabeno, P., Strausz, D.,
1166 Wisegarver, E., and Wood, K.: Seasonal and interannual variability of nitrate in the eastern
1167 Chukchi Sea: Transport and winter replenishment, Deep-Sea Res. Part II Top. Stud. Oceanogr.,
1168 177, 104807, <https://doi.org/10.1016/j.dsr2.2020.104807>, 2020.
1169
1170 National Academies of Sciences, Engineering and Medicine: Valuing Climate Damages:
1171 Updating Estimation of the Social Cost of Carbon Dioxide (Washington DC: The National
1172 Academies Press) <https://doi.org/10.17226/24651>, 2017.
1173
1174 Newton, J. A., Feely, R. A., Jewett, E. B., Williamson, P., and Mathis, J.: Global ocean
1175 acidification observing network: requirements and governance plan, GOA-ON, Washington, 61
1176 pp., http://www.goa-on.org/docs/GOA-ON_plan_print.pdf, 2015.
1177

1178 Orr, J. C.: Recent and future changes in ocean carbonate chemistry, in: Ocean acidification,
1179 edited by: Gattuso, J.-P. and Hansson, L., Oxford University Press, Oxford, 41–66, 2011.

1180

1181 Orr, J. C., Epitalon, J.-M., Dickson, A. G., and Gattuso, J.-P.: Routine uncertainty propagation
1182 for the marine carbon dioxide system, *Mar. Chem.*, 207, 84–107,
1183 <https://doi.org/10.1016/j.marchem.2018.10.006>, 2018.

1184

1185 Orr, J. C., Kwiatkowski, L., and Pörtner, H. O.: Arctic Ocean annual high in pCO₂ could shift
1186 from winter to summer, *Nature*, 610, 94–100, <https://doi.org/10.1038/s41586-022-05205-y>,
1187 2022.

1188

1189 Ouyang, Z., Collins, A., Li, Y., Qi, D., Arrigo, K. R., Zhuang, Y., Nishino, S., Humphreys, M.
1190 P., Kosugi, N., Murata, A., Kirchman, D. L., Chen, L., Chen, J. and Cai, W.-J.: Seasonal Water
1191 Mass Evolution and Non-Redfield Dynamics Enhance CO₂ Uptake in the Chukchi Sea. *Journal*
1192 *of Geophysical Research: Oceans* 127, e2021JC018326,
1193 <https://doi.org/10.1029/2021JC018326>, 2022.

1194

1195 Payne, C. M., Bianucci, L., van Dijken, G. L., and Arrigo, K. R.: Changes in Under-Ice Primary
1196 Production in the Chukchi Sea From 1988 to 2018, *J. Geophys. Res. Oceans*, 126,
1197 e2021JC017483, <https://doi.org/10.1029/2021JC017483>, 2021.

1198

1199 Perez, F. F. and Fraga, F.: Association constant of fluoride and hydrogen ions in seawater, *Mar.*
1200 *Chem.*, 21, 161–168, [https://doi.org/10.1016/0304-4203\(87\)90036-3](https://doi.org/10.1016/0304-4203(87)90036-3), 1987.

1201

1202 Pipko, I. I., Semiletov, I. P., Tishchenko, P. Y., Pugach, S. P. and Christensen, J. P.: Carbonate
1203 chemistry dynamics in Bering Strait and the Chukchi Sea. *Progress in Oceanography* 55, 77–94,
1204 [https://doi.org/10.1016/S0079-6611\(02\)00071-X](https://doi.org/10.1016/S0079-6611(02)00071-X), 2002.

1205

1206 Qi, D., Chen, L., Chen, B., Gao, Z., Zhong, W., Feely, R. A., Anderson, L. G., Sun, H., Chen, J.,
1207 Chen, M., Zhan, L., Zhang, Y., and Cai, W.-J.: Increase in acidifying water in the western Arctic
1208 Ocean, *Nat. Clim. Change*, 7, 195–199, <https://doi.org/10.1038/nclimate3228>, 2017.

1209

1210 Qi, D., Ouyang, Z., Chen, L., Wu, Y., Lei, R., Chen, B., Feely, R. A., Anderson, L. G., Zhong,
1211 W., Lin, H., Polukhin, A., Zhang, Y., Zhang, Y., Bi, H., Lin, X., Luo, Y., Zhuang, Y., He, J.,
1212 Chen, J., and Cai, W. J.: Climate change drives rapid decadal acidification in the Arctic Ocean
1213 from 1994 to 2020, *Science*, 377, 1544–1550, <https://doi.org/10.1126/science.abo0383>, 2022a.

1214

1215 Qi, D., Wu, Y., Chen, L., Cai, W.-J., Ouyang, Z., Zhang, Y., Anderson, L. G., Feely, R. A.,
1216 Zhuang, Y., Lin, H., Lei, R., and Bi, H.: Rapid acidification of the Arctic Chukchi Sea waters
1217 driven by anthropogenic forcing and biological carbon recycling, *Geophysical Research Letter*,
1218 49(4), e2021GL097246, <https://doi.org/10.1029/2021GL097246>, 2022b.

1219

1220 Raimondi, L., Matthews, J. B. R., Atamanchuk, D., Azetsu-Scott, K., and Wallace, D.: The
1221 internal consistency of the marine carbon dioxide system for high latitude shipboard and in situ
1222 monitoring, *Mar. Chem.*, 213, 49–70, <https://doi.org/10.1016/j.marchem.2019.03.001>, 2019.

1223

1224 Rantanen, M., Karpechko, A. Y., Lipponen, A., Nordling, K., Hyvärinen, O., Ruosteenoja, K.,
1225 Vihma, T., and Laaksonen, A.: The Arctic has warmed nearly four times faster than the globe
1226 since 1979, *Commun. Earth Environ.*, 3, 1–10, <https://doi.org/10.1038/s43247-022-00498-3>,
1227 2022.

1228

1229 Rheuban, J. E., Doney, S. C., McCorkle, D. C. and Jakuba, R. W. Quantifying the Effects of
1230 Nutrient Enrichment and Freshwater Mixing on Coastal Ocean Acidification. *Journal of*
1231 *Geophysical Research: Oceans* 124(12), 9085–9100,
1232 <https://doi.org/10.1029/2019JC015556>, 2019.

1233

1234 Rysgaard, S., Glud, R. N., Sejr, M. K., Bendtsen, J., and Christensen, P. B.: Inorganic carbon
1235 transport during sea ice growth and decay: A carbon pump in polar seas, *J. Geophys. Res.*, 112,
1236 C03016, <https://doi.org/10.1029/2006JC003572>, 2007.

1237

1238 Rysgaard, S., Glud, R. N., Lennert, K., Cooper, M., Halden, N., Leakey, R. J. G., Hawthorne, F.
1239 C., and Barber, D.: Ikaite crystals in melting sea ice – implications for pCO₂ and pH levels in
1240 Arctic surface waters, *The Cryosphere*, 6, 901–908, <https://doi.org/10.5194/tc-6-901-2012>, 2012.

1241

1242 Sakamoto, C. M., Johnson, K. S., and Coletti, L. J.: Improved algorithm for the computation of
1243 nitrate concentrations in seawater using an in situ ultraviolet spectrophotometer, *Limnol.*
1244 *Oceanogr. Methods*, 7, 132–143, <https://doi.org/10.4319/lom.2009.7.132>, 2009.

1245

1246 Sandy, S. J., Danielson, S. L., and Mahoney, A. R.: Automating the Acoustic Detection and
1247 Characterization of Sea Ice and Surface Waves, *J. Mar. Sci. Eng.*, 10, 1577,
1248 <https://doi.org/10.3390/jmse10111577>, 2022.

1249

1250 Sarmiento, J. L. and Gruber, N.: *Ocean Biogeochemical Dynamics*, Princeton University Press,
1251 Princeton, NJ, 526 pp., 2006.

1252

1253 Seabird. Application Note 31: Computing temperature and conductivity slope and offset
1254 correction coefficients from lab calibration and salinity bottle samples. [my.hach.com/asset-
1255 get.download.jsa?id=54627861537](http://my.hach.com/asset-get.download.jsa?id=54627861537), accessed 20 June 2016.

1256

1257 Seabird. Module 28. Advanced Biogeochemical Processing, [www.seabird.com/cms-
1258 portals/seabird_com/cms/documents/training/Module28_Advanced_Biogeochem_Processing.pdf](http://www.seabird.com/cms-portals/seabird_com/cms/documents/training/Module28_Advanced_Biogeochem_Processing.pdf)
1259 . Accessed 30 May 2023.

1260

1261 Seferian, R.: CNRM-CERFACS CNRM-ESM2-1 model output prepared for CMIP6
1262 AerChemMIP. doi:10.22033/ESGF/CMIP6.1389, 2019.

1263

1264 Semiletov, I., Pipko, I., Gustafsson, Ö., Anderson, L. G., Sergienko, V., Pugach, S., Dudarev, O.,
1265 Charkin, A., Gukov, A., Bröder, L., Andersson, A., Spivak, E., and Shakhova, N.: Acidification
1266 of East Siberian Arctic Shelf waters through addition of freshwater and terrestrial carbon. *Nature
1267 Geosci* 9, 361–365, <https://doi.org/10.1038/ngeo2695>, 2016.

1268

1269 Serreze, M. C. and Barry, R. G.: Processes and impacts of Arctic amplification: A research
1270 synthesis, *Glob. Planet. Change*, 77, 85–96, <https://doi.org/10.1016/j.gloplacha.2011.03.004>,
1271 2011.

1272

1273 Serreze, M. C. and Francis, J. A.: The Arctic amplification debate, *Clim. Change*, 76, 241–264,
1274 <https://doi.org/10.1007/s10584-005-9017-y>, 2006.

1275

1276 Serreze, M. C., Crawford, A. D., Stroeve, J. C., Barrett, A. P., and Woodgate, R. A.: Variability,
1277 trends, and predictability of seasonal sea ice retreat and advance in the Chukchi Sea, *J. Geophys.*
1278 *Res. Oceans*, 121, 7308–7325, <https://doi.org/10.1002/2016JC011977>, 2016.

1279

1280 Sharp, J. D., Pierrot, D., Humphreys, M. P., Epitalon, J.-M., Orr, J. C., Lewis, E. R., and
1281 Wallace, D. W. R.: CO2SYSv3 for MATLAB, <https://doi.org/10.5281/zenodo.7552554>, 2023.

1282

1283 Shu, Q., Wang, Q., Årthun, M., Wang, S., Song, Z., Zhang, M., and Qiao, F: Arctic Ocean
1284 Amplification in a warming climate in CMIP6 models. *Science Advances*, 8(30), eabn9755.
1285 <https://doi.org/10.1126/sciadv.abn9755>, 2022.

1286

1287 Stabeno, P. J., Mordy, C. W. and Sigler, M. F.: Seasonal patterns of near-bottom chlorophyll
1288 fluorescence in the eastern Chukchi Sea: 2010–2019. *Deep Sea Research Part II: Topical Studies*
1289 in *Oceanography* 177, 104842, <https://doi.org/10.1016/j.dsr2.2020.104842>, 2020.

1290

1291 Stackpoole, S., Butman, D., Clow, D., Verdin, K., Gaglioti, B., and Striegl, R. G.: Carbon burial,
1292 transport, and emission from inland aquatic ecosystems in Alaska, USGS Prof. Pap., 1826, 159–
1293 188, <https://doi.org/10.3133/pp1826>, 2016.

1294

1295 Stackpoole, S. M., Butman, D., Clow, D. W., Verdin, K. L., Gaglioti, B. V., Genet, H., and
1296 Striegl, R. G.: Inland waters and their role in the carbon cycle of Alaska, *Ecol. Appl.*, 27, 1403–
1297 1420, <http://onlinelibrary.wiley.com/doi/10.1002/eap.1552/full>, 2017.

1298

1299 Silvers, L., Blanton, C., McHugh, C., John, J. G., Radhakrishnan, A., Rand, K., Balaji, V.,
1300 Dupuis, C., Durachta, J., Guo, H., Hemler, R., Lin, P., Nikonov, S., Paynter, D. J., Poshay, J.,
1301 Vahlenkamp, H., Wilson, C., Wyman, B., Robinson, T., Zeng, Y. and Zhao, M.: NOAA-GFDL
1302 GFDL-CM4 model output prepared for CMIP6 CMIP. doi:10.22033/ESGF/CMIP6.1641, 2018.

1303

1304 Stroeve, J. C., Serreze, M. C., Holland, M. M., Kay, J. E., Malanik, J., and Barrett, A. P.: The
1305 Arctic's rapidly shrinking sea ice cover: a research synthesis, *Clim. Change*, 110, 1005–1027,
1306 <https://doi.org/10.1007/s10584-011-0101-1>, 2011.

1307

1308 Stroeve, J. C., Markus, T., Boisvert, L., Miller, J., and Barrett, A.: Changes in Arctic melt season
1309 and implications for sea ice loss, *Geophys. Res. Lett.*, 41, 1216–1225,
1310 <https://doi.org/10.1002/2013GL058951>, 2014.

1311

1312 Stumpp, M., Hu, M. Y., Melzner, F., Gutowska, M. A., Dorey, N., Himmerkus, N., Holtmann,
1313 W. C., Dupont, S. T., Thorndyke, M. C., and Bleich, M.: Acidified seawater impacts sea urchin

1314 larvae pH regulatory systems relevant for calcification, Proc. Natl. Acad. Sci. USA, 109, 18192–
1315 18197, <https://doi.org/10.1073/pnas.1209174109>, 2012.

1316

1317 Sulpis, O., Lauvset, S. K., and Hagens, M.: Current estimates of K_1^* and K_2^* appear inconsistent
1318 with measured CO₂ system parameters in cold oceanic regions, Ocean Sci., 16, 847–862,
1319 <https://doi.org/10.5194/os-16-847-2020>, 2020.

1320

1321 Takahashi, T., Sutherland, S. C., Sweeney, C., Poisson, A., Metzl, N., Tilbrook, B., Bates, N.,
1322 Wanninkhof, R., Feely, R. A., Sabine, C., Olafsson, J., and Nojiri, Y.: Global sea–air CO₂ flux
1323 based on climatological surface ocean pCO₂, and seasonal biological and temperature effects,
1324 Deep Sea Res. Part II Top. Stud. Oceanogr., 49, 1601–1622, [https://doi.org/10.1016/S0967-0645\(02\)00003-6](https://doi.org/10.1016/S0967-0645(02)00003-6), 2002.

1326

1327 Terhaar, J., Torres, O., Bourgeois, T., and Kwiatkowski, L.: Arctic Ocean acidification over the
1328 21st century co-driven by anthropogenic carbon increases and freshening in the CMIP6 model
1329 ensemble, Biogeosciences, 18, 2221–2240, <https://doi.org/10.5194/bg-18-2221-2021>, 2021.

1330

1331 Thomsen, J., Casties, I., Pansch, C., Körtzinger, A., and Melzner, F.: Food availability outweighs
1332 ocean acidification effects in juvenile *Mytilus edulis*: laboratory and field experiments, Glob.
1333 Change Biol., 19, 1017–1027, <https://doi.org/10.1111/gcb.12109>, 2013.

1334

1335 Thor, P. and Dupont, S.: Transgenerational effects alleviate severe fecundity loss during ocean
1336 acidification in a ubiquitous planktonic copepod, *Glob. Change Biol.*, 21, 2261–2271,
1337 <https://doi.org/10.1111/gcb.12815>, 2015.

1338

1339 Tian, F., Pickart, R.S., Lin, P., Pacini, A., Moore, G.W.K., Stabeno, P., Weingartner, T., Itoh,
1340 M., Kikuchi, T., Dobbins, E. and Bell, S.: Mean and seasonal circulation of the eastern Chukchi
1341 Sea from moored timeseries in 2013–2014. *Journal of Geophysical Research: Oceans*, 126(5),
1342 p.e2020JC016863, 2021.

1343

1344 Tunnicliffe, V., Davies, K. T. A., Butterfield, D. A., Embley, R. W., Rose, J. W., and Chadwick
1345 Jr, W. W.: Survival of mussels in extremely acidic waters on a submarine volcano, *Nat. Geosci.*,
1346 2, 344–348, <https://doi.org/10.1038/ngeo500>, 2009.

1347

1348 Van Straalen, M. N.: Peer Reviewed: Ecotoxicology Becomes Stress Ecology, *Environ. Sci.*
1349 *Technol.*, 37, 324A-330A, <https://doi.org/10.1021/es0325720>, 2003.

1350

1351 Vargas, C. A., Lagos, N. A., Lardies, M. A., Duarte, C., Manríquez, P. H., Aguilera, V. M.,
1352 Broitman, B., Widdicombe, S., and Dupont, S.: Species-specific responses to ocean acidification
1353 should account for local adaptation and adaptive plasticity, *Nat Ecol Evol* 1, 0084,
1354 <https://doi.org/10.1038/s41559-017-0084>, 2017.

1355

1356 Vargas, C. A., Cuevas, L. A., Broitman, B. R., San Martin, V. A., Lagos, N. A., Gaitán-Espitia,
1357 J. D., and Dupont, S.: Upper environmental pCO₂ drives sensitivity to ocean acidification in

1358 marine invertebrates, *Nat. Clim. Change*, 12, 200–207, <https://doi.org/10.1038/s41558-021-01269-2>, 2022.

1360

1361 Ventura, A., Schulz, S., and Dupont, S.: Maintained larval growth in mussel larvae exposed to

1362 acidified under-saturated seawater, *Sci. Rep.*, 6, 23728, <https://doi.org/10.1038/srep23728>, 2016.

1363

1364 Vergara-Jara, M. J., DeGrandpre, M. D., Torres, R., Beatty, C. M., Cuevas, L. A., Alarcón, E.

1365 and Iriarte, J. L: Seasonal Changes in Carbonate Saturation State and Air-Sea CO₂ Fluxes During

1366 an Annual Cycle in a Stratified-Temperate Fjord (Reloncaví Fjord, Chilean Patagonia). *Journal*

1367 *of Geophysical Research: Biogeosciences* 124, 2851–2865,

1368 <https://doi.org/10.1029/2019JG005028>, 2019.

1369

1370 Watanabe, Y. W., Li, B. F., Yamasaki, R., Yunoki, S., Imai, K., Hosoda, S., and Nakano, Y.:

1371 Spatiotemporal changes of ocean carbon species in the western North Pacific using

1372 parameterization technique, *J. Oceanogr.*, 76, 155–167, <https://doi.org/10.1007/s10872-019-00532-7>, 2020.

1374

1375 Williams, N. L., Juranek, L. W., Johnson, K. S., Feely, R. A., Riser, S. C., Talley, L. D., Russell,

1376 J. L., Sarmiento, J. L., and Wanninkhof, R.: Empirical algorithms to estimate water column pH

1377 in the Southern Ocean, *Geophys. Res. Lett.*, 43, 3415–3422,

1378 <https://doi.org/10.1002/2016GL068539>, 2016.

1379

1380 Wieners, K.-H., Giorgetta, M., Jungclaus, J., Reick, C., Esch, M., Bittner, M., Legutke, S.,
1381 Schupfner, M., Wachsmann, F., Gayler, V., Haak, H., de Vrese, P., Raddatz, T., Mauritsen, T.,
1382 von Storch, J.-S., Behrens, J., Brovkin, V., Claussen, M., Crueger, T., Fast, I., Fiedler, S.,
1383 Hagemann, S., Hohenegger, C., Jahns, T., Kloster, S., Kinne, S., Lasslop, G., Kornblueh, L.,
1384 Marotzke, J., Matei, D., Meraner, K., Mikolajewicz, U., Modali, K., Müller, W., Nabel, J., Notz,
1385 D., Peters-von Gehlen, K., Pincus, R., Pohlmann, H., Pongratz, J., Rast, S., Schmidt, H., Schnur,
1386 R., Schulzweida, U., Six, K., Stevens, B., Voigt, A. and Roeckner, E.: MPI-M MPI-ESM1.2-LR
1387 model output prepared for CMIP6 CMIP historical. doi:10.22033/ESGF/CMIP6.6595, 2019.
1388
1389 Wolf-Gladrow, D. A., Zeebe, R. E., Klaas, C., Körtzinger, A., and Dickson, A. G.: Total
1390 alkalinity: The explicit conservative expression and its application to biogeochemical processes,
1391 Mar. Chem., 106, 287–300, <https://doi.org/10.1016/j.marchem.2007.01.006>, 2007.
1392
1393 Wood, K. R., Bond, N. A., Danielson, S. L., Overland, J. E., Salo, S. A., Stabeno, P. J., and
1394 Whitefield, J.: A decade of environmental change in the Pacific Arctic region, Prog. Oceanogr.,
1395 136, 12–31, <https://doi.org/10.1016/j.pocean.2015.05.005>, 2015.
1396
1397 Woosley, R. J.: Evaluation of the temperature dependence of dissociation constants for the
1398 marine carbon system using pH and certified reference materials, Marine Chemistry,
1399 229, 103914, <https://doi.org/10.1016/j.marchem.2020.103914>, 2021.
1400
1401 Woosley, R. J., Millero, F. J., and Takahashi, T.: Internal consistency of the inorganic carbon
1402 system in the Arctic Ocean, Limnol. Oceanogr. Methods, 15, 887–896,
1403 <https://doi.org/10.1002/lom3.10208>, 2017.

1404

1405 Woosley, R. J. and Millero, F. J.: Freshening of the western Arctic negates anthropogenic carbon
1406 uptake potential, Limnol. Oceanogr., 65, 1834–1846, <https://doi.org/10.1002/lno.11421>, 2020.

1407

1408 Yamamoto-Kawai, M., McLaughlin, F. A., Carmack, E. C., Nishino, S., and Shimada, K.:
1409 Aragonite undersaturation in the Arctic Ocean: effects of ocean acidification and sea ice melt,
1410 Science, 326, 1098–1100, <https://doi.org/10.1126/science.1174190>, 2009.

1411

1412 Zeng, J., Chen, M., Zheng, M., Hu, W., and Qiu, Y.: A potential nitrogen sink discovered in the
1413 oxygenated Chukchi Shelf waters of the Arctic, Geochem. Trans., 18, 5,
1414 <https://doi.org/10.1186/s12932-017-0043-2>, 2017.

1415

1416

1417 **Tables**

1418 **Table 1.** Chukchi Ecosystem Observatory location and instrument sampling frequency. Sensor
1419 type and parameter measured (italicized) shown in top row. Values in parenthesis indicate the
1420 number of measurements averaged over the measurement interval window.

Deployment	Latitude	Longitude	SUNA <i>NO₃</i>	HydroC CO ₂ <i>pCO₂</i>	SBE16 <i>CTD+</i>	SBE37 <i>CTD</i>	SeaFET <i>pH</i>	SBE63 <i>O₂</i>
2016-2017	71.5996	-161.5184	1 h	12 h (300/5 min)*	1 h	-	-	-
2017-2018	71.5997	-161.5189	1 h	12 h (5/5 min)	2 h	2 h	2 h (30/5 min)	2 h
2018-2019	71.5999	-161.5281	1 h	24 h (5/5 min)	1 h	2 h*	-	2 h*

2019-2020	71.5997	-161.5275	1 h	12 h (5/5 min)	2 h	-	-	-
* indicates the sensor did not return data over the whole year due to battery failure								
CTD+ indicates ancillary data was available with the SBE16 file (e.g., chlorophyll fluorescence)								

1421

1422

1423

1424 **Table 2.** Evaluation of $\text{pH}_{\text{SeaFET}}$ and pH^{est} using reference pH from nearby discrete samples

1425 ($\text{pH}^{\text{disc calc}}$). Uncertainty, u_c , is the propagated combined standard uncertainty from *errors.m* (Orr

1426 et al., 2018). $\text{pH}_{\text{SeaFET}}$ and pH^{est} were interpolated to the discrete timestamp. Figure S1 for

1427 visualization of reference values.

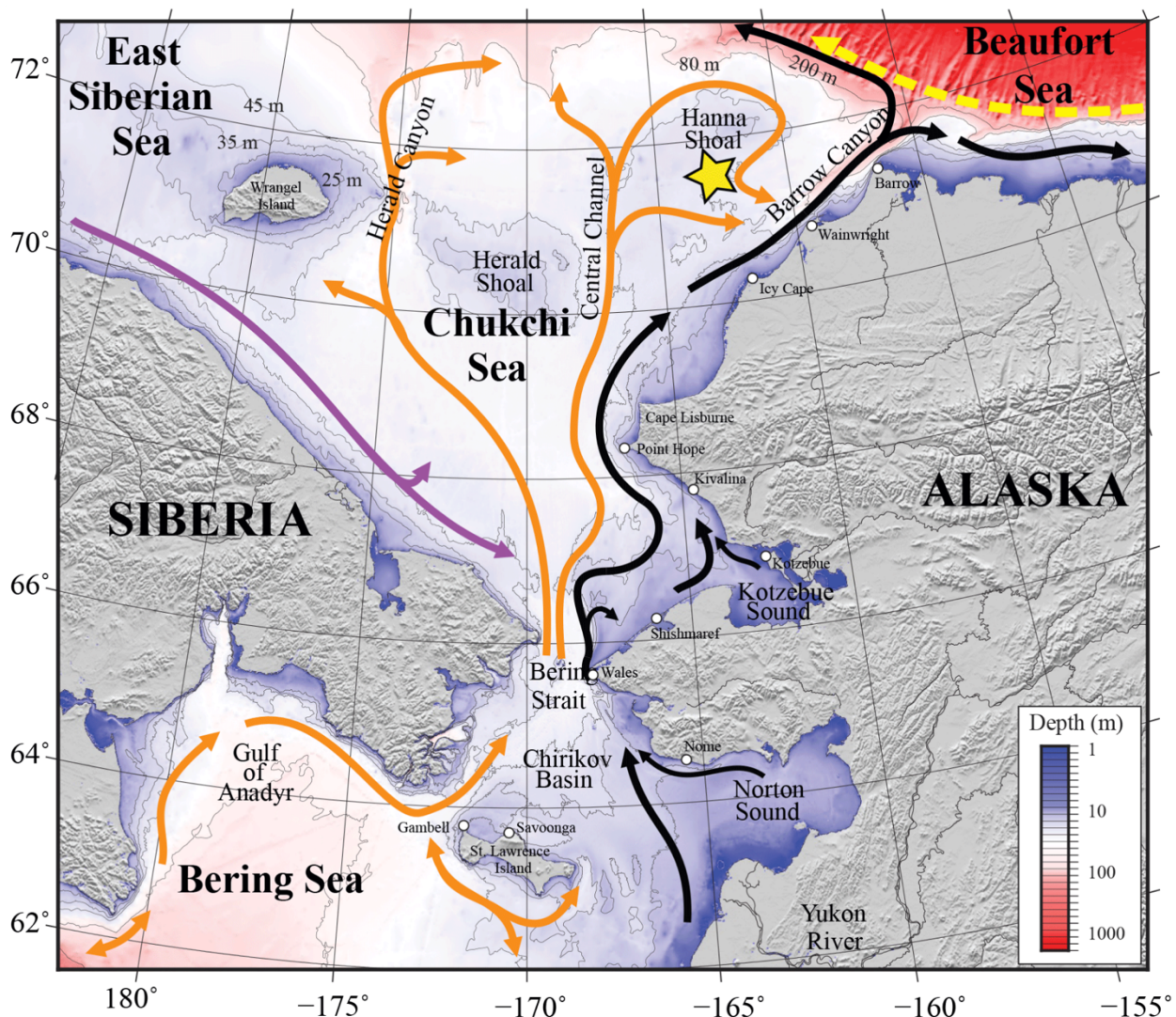
1428

Date	Cruise	Cast No.	Distance (km)	$\text{pH}^{\text{disc calc}} \pm u_c$	Anomaly ($\text{pH}^{\text{est}} - \text{pH}^{\text{disc calc}}$)	Anomaly ($\text{pH}_{\text{SeaFET}} - \text{pH}^{\text{disc calc}}$)	Source
2017-09-10	HLY1702	127	0.52	8.0123 ± 0.0166	-0.0450*	-0.0354	Cross et al., 2020a
2019-08-11	HLY1901	39	3.75	7.6423 ± 0.012	0.0079*	-	Cross et al., 2021
2019-08-19	OS1901	33	0.27	7.7367 ± 0.0145	-0.0200	-	unpublished

* indicates $\text{pH}^{\text{disc calc}}$ was interpolated to mooring depth

1429

1430

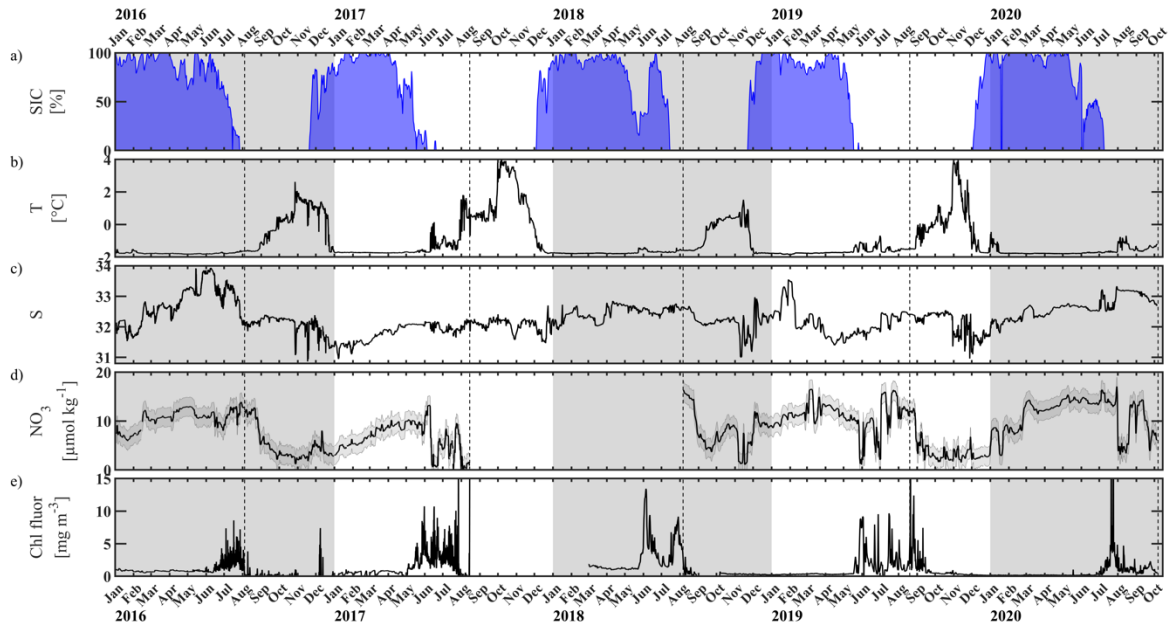
1431 **Figures**

1432

1433 **Figure 1. Map of the study area.** Bathymetry of the Chukchi, northern Bering, East Siberian
 1434 and eastern Beaufort seas is shown in color. The Chukchi Ecosystem Observatory (CEO)
 1435 location near Hanna Shoal is marked with a yellow star. General circulation patterns are shown
 1436 with arrows: black – Alaskan Coastal Water and Alaskan Coastal Current, dividing into the
 1437 Shelf-break Jet (right) and Chukchi Slope Current (left, Corlett and Pickart, (2017)); orange –
 1438 Anadyr, Bering, and Chukchi Seawater; purple – Siberian Coastal Current; yellow – Beaufort
 1439 Gyre boundary current. Figure is from Hauri et al. (2018).

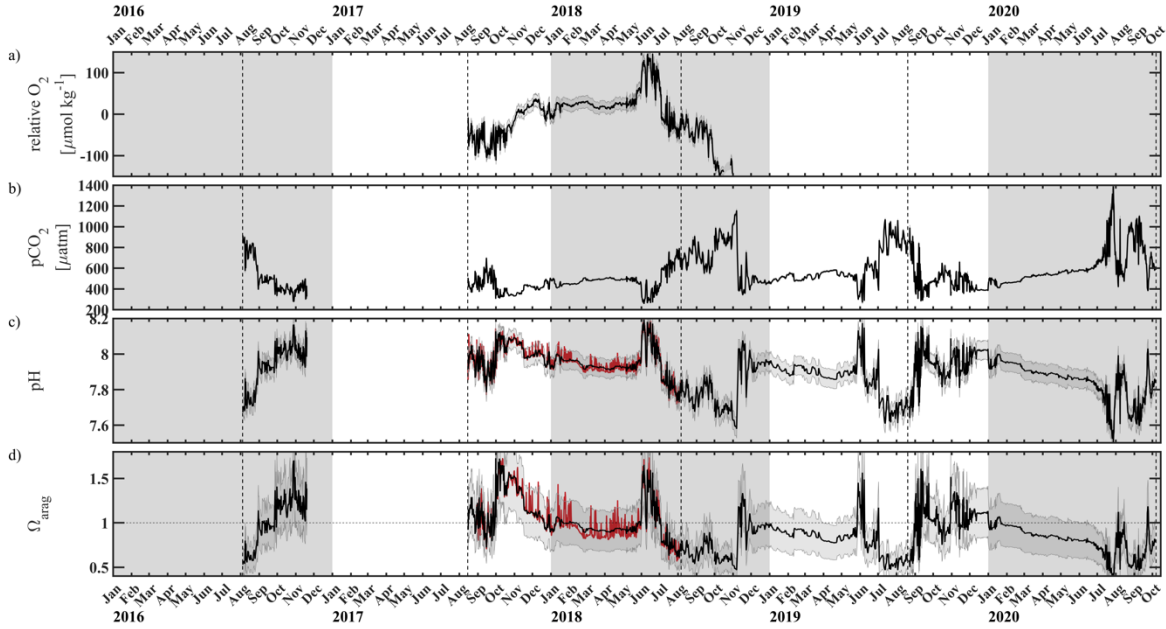
1440

1441



1442

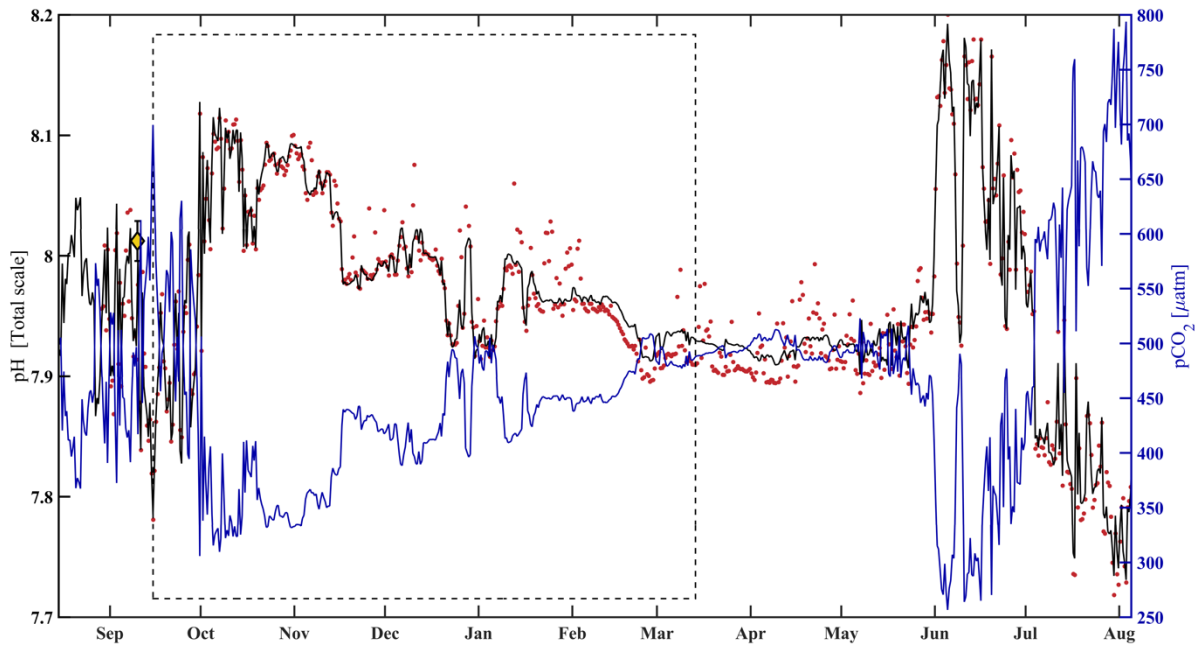
1443 **Figure 2. Chukchi Ecosystem Observatory timeseries from 2016 through 2020.** a) sea ice
 1444 concentration (blue shading to highlight coverage, %; DiGirolamo et al., 2022), b) temperature
 1445 ($^{\circ}\text{C}$), c) salinity, d) NO_3 with uncertainty envelope ($\mu\text{mol kg}^{-1}$), and e) chlorophyll fluorescence
 1446 (mg m^{-3}). Years are indicated by alternating gray and white background shading. The vertical
 1447 dotted gray lines indicate the mooring turn around timing.



1448

1449 **Figure 3. Chukchi Ecosystem Observatory timeseries from 2016 through 2020, part 2.** a)
1450 relative dissolved oxygen with uncertainty envelope (relative to the mean; $\mu\text{mol kg}^{-1}$), b) $p\text{CO}_2$
1451 with uncertainty envelope (μatm ; Hauri and Irving, 2023a), c) pH with uncertainty envelope
1452 (pH^{est} in black, $\text{pH}_{\text{SeaFET}}$ in red; Hauri and Irving 2023b), and d) aragonite saturation state with
1453 uncertainty envelope ($\Omega_{\text{arag}}(p\text{CO}_2, \text{pH}^{\text{est}})$ in black; $\Omega_{\text{arag}}(p\text{CO}_2, \text{pH}_{\text{SeaFET}})$ in red). Years are
1454 indicated by alternating gray and white backgrounds. The vertical dotted gray lines indicate the
1455 mooring turn around timing.

1456



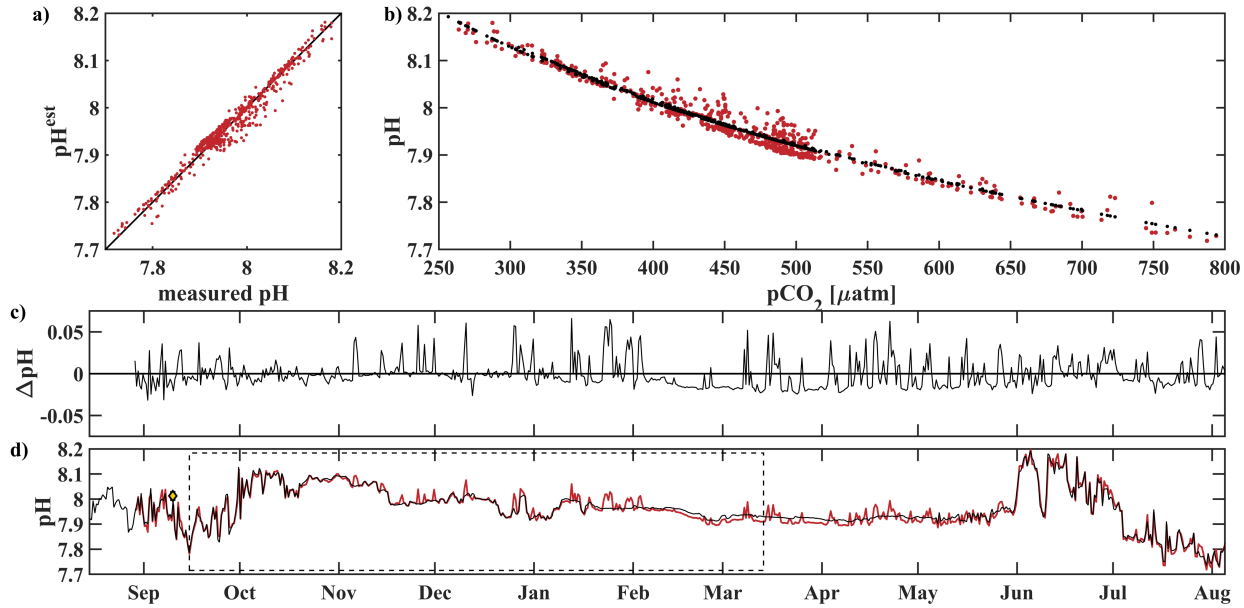
1457

1458

1459 **Figure 4. HydroC $p\text{CO}_2$ and pH highlighting mirrored trend from mid-August 2017 to**
 1460 **beginning of August 2018.** Measured pH ($\text{pH}_{\text{SeaFET}}$, red dots) is interpolated onto the HydroC
 1461 $p\text{CO}_2$ timestamp (blue), and pH^{est} is shown as the solid black line. The dashed box shows the
 1462 period over which pH^{est} was trained. The yellow faced diamond with error bars show reference
 1463 $\text{pH}^{\text{disc,calc}} \pm u_c$ (Table 2; Cross et al., 2020a; Orr et al., 2018).

1464

1465



1466

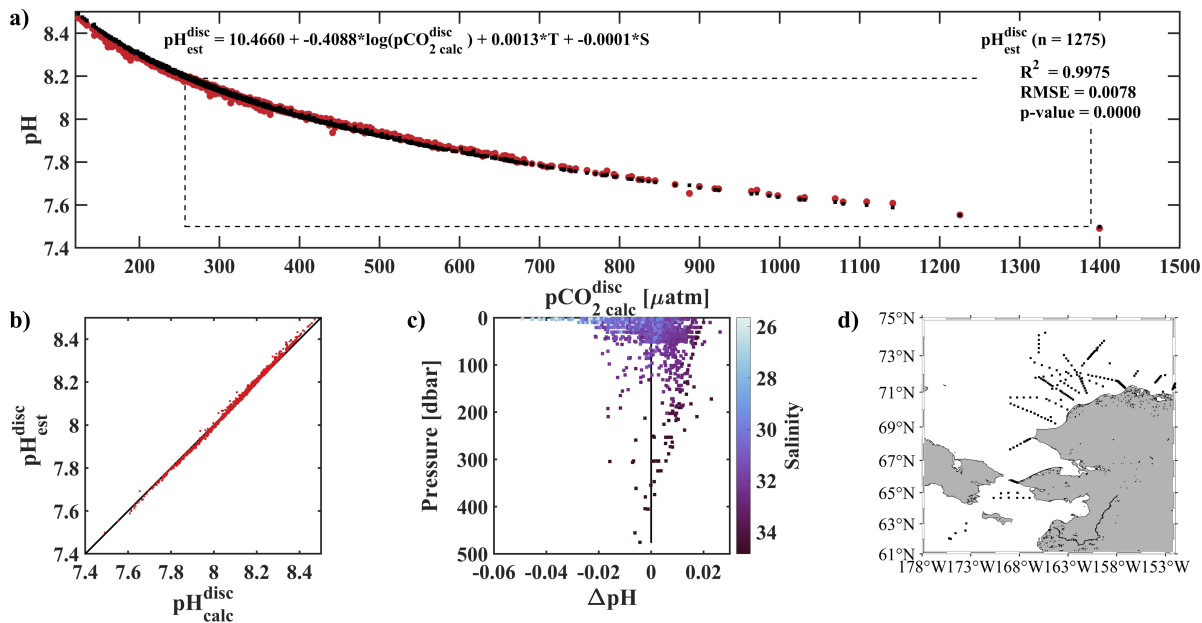
1467 **Figure 5. Performance of the pH algorithm.** (a) pH_{SeaFET} vs pH^{est} with black line highlighting
1468 1:1 ratio, (b) $p\text{CO}_2$ vs pH_{SeaFET} (red) and $p\text{CO}_2$ vs pH^{est} (black), (c) residual pH (pH_{SeaFET} –
1469 pH^{est}), and (d) pH_{SeaFET} (red) and pH^{est} (black) vs. time, with dashed box highlighting the period
1470 over which pH^{est} was trained (15 September - 14 March 2017), and the yellow faced diamond
1471 with error bars showing reference pH^{disc}_{calc} $\pm u_c$ (Table 2; Cross et al., 2020).

1472

1473

1474

1475

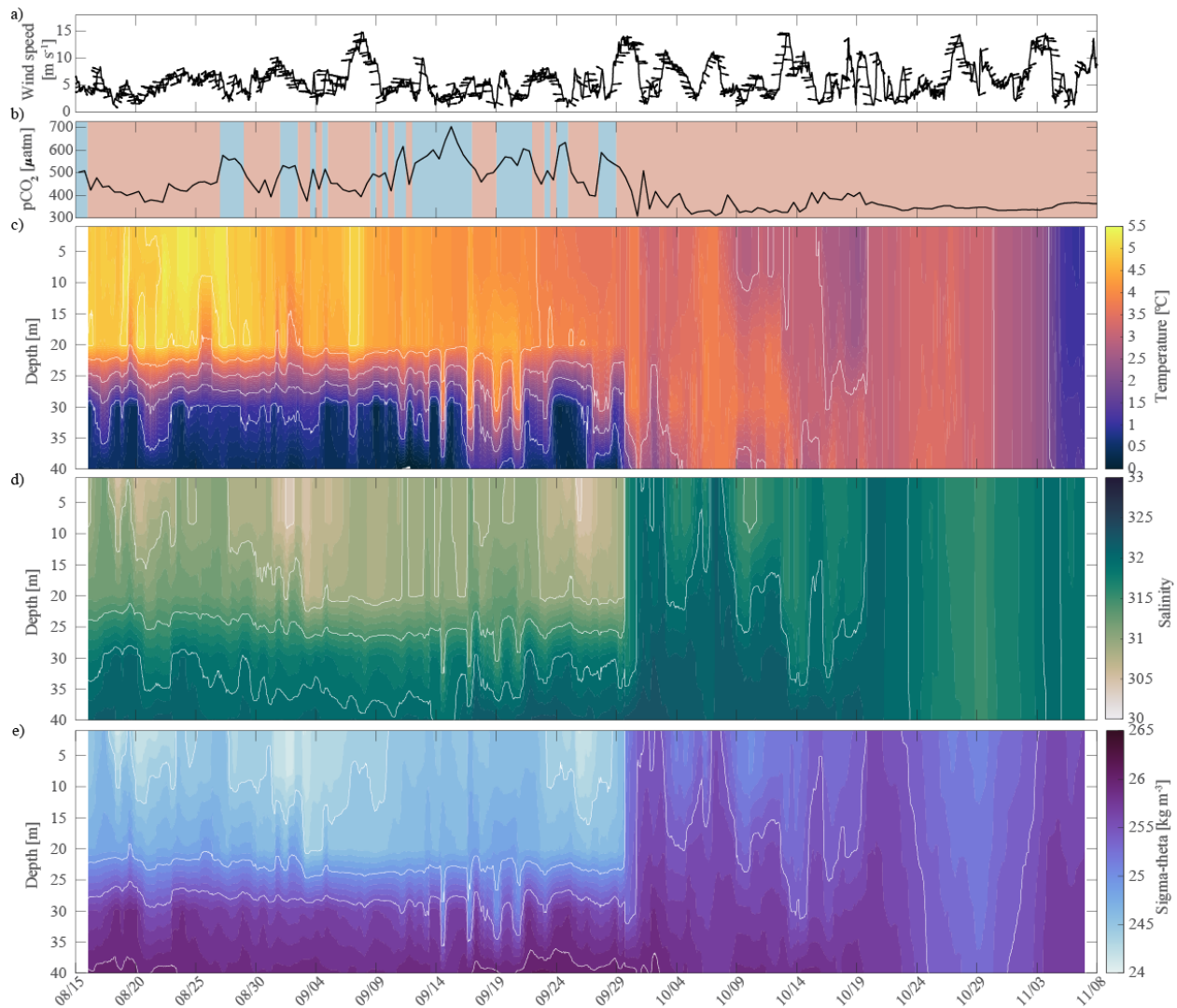


1476

1477 **Figure 6. Evaluation of the pH algorithm.** pH^{est} evaluation with $\text{pH}^{\text{disc,calc}}$ from discrete
 1478 samples collected during 4 cruises in the fall or early winter (August - November) of 2017-2020
 1479 and $\text{pH}^{\text{disc,est}}$ from our linear regression model (Equation 2). (a) $p\text{CO}_2^{\text{disc,calc}}$ (TA, DIC) vs pH (red
 1480 $\text{pH}^{\text{disc,calc}}$ and black $\text{pH}^{\text{disc,est}}$) with dashed black box showing the range of pH and $p\text{CO}_2$ observed
 1481 at the CEO at 33 m depth, (b) $\text{pH}^{\text{disc,calc}}$ vs $\text{pH}^{\text{disc,est}}$ with black 1:1 ratio, (c) residual pH ($\text{pH}^{\text{disc,calc}} -$
 1482 $\text{pH}^{\text{disc,est}}$) vs depth with color shading by salinity and black vertical line at 0, and (d) map showing
 1483 the locations of the 1275 discrete water samples used for evaluation (Monacci et al., 2022; Cross
 1484 et al., 2021; 2020a; 2020b).

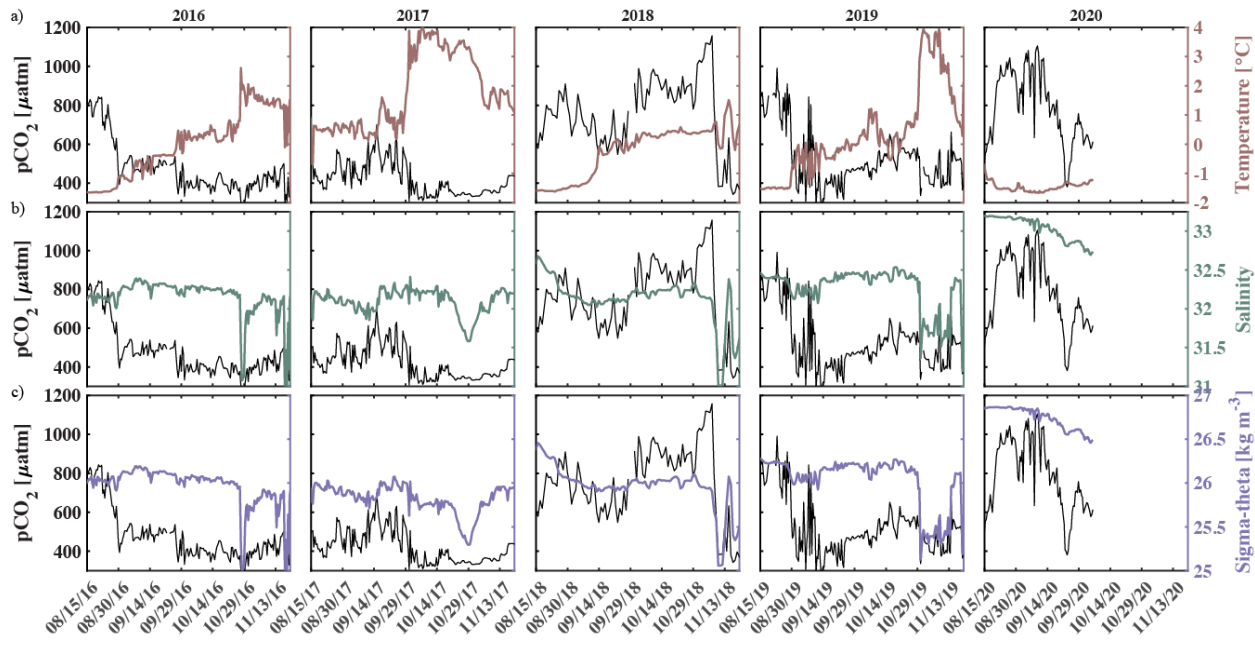
1485

1486



1487

1488 **Figure 7. Water column structure from late summer 2017 to freeze up.** Profiles of a) wind
 1489 speed and direction (arrows pointing downwind) from the NOAA-operated Wiley Post-Will
 1490 Rogers Memorial Airport, b) $p\text{CO}_2$ (μatm) with blue background indicating the water was
 1491 undersaturated regarding aragonite ($\Omega_{\text{arag}} < 1$) and red shading indicating aragonite
 1492 oversaturation ($\Omega_{\text{arag}} \geq 1$), c) temperature ($^{\circ}\text{C}$), d) salinity, and e) sigma-theta (kg m^{-3}).
 1493 Temperature (c) and salinity (d) were measured at 8, 20, 30, and 40 m by the Chukchi Ecosystem
 1494 Observatory freeze-up detection mooring deployed in fall 2017. Density was calculated with the
 1495 TEOS-10 GSW Oceanographic Toolbox (McDougall and Baker, 2011).



1496

1497 **Figure 8. Impact of water column mixing on $p\text{CO}_2$.** Timeseries of $p\text{CO}_2$ (black, left axis) and
 1498 a) temperature (maroon, right axis), b) salinity (green, right axis), and c) density (purple, right
 1499 axis) for 15 August to 1 December in 2016 -2020 measured at ~33m depth at the Chukchi Sea
 1500 Ecosystem Observatory.

1501

1502

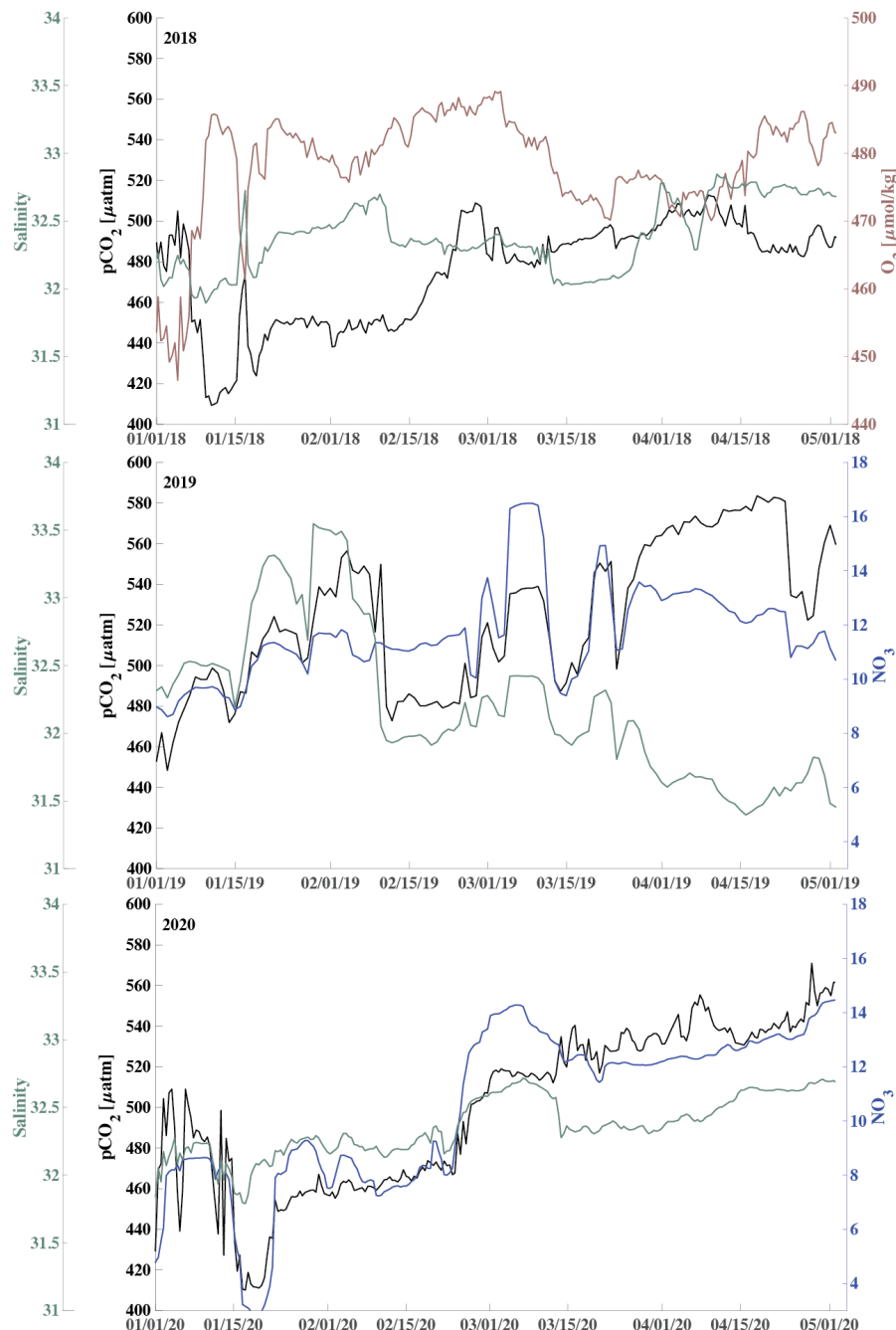
1503

1504

1505

1506

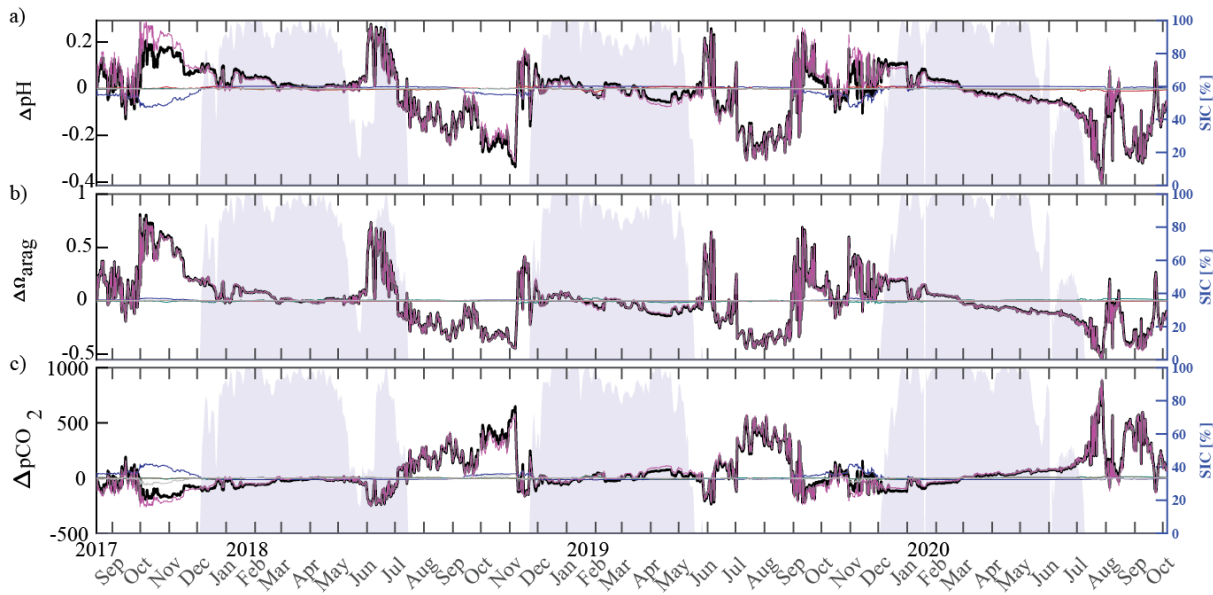
1507



1508

1509 **Figure 9. Respiration under the sea ice.** Timeseries of $p\text{CO}_2$ (black) and salinity (green, left
 1510 axis), and oxygen (O_2 , $\mu\text{mol kg}^{-1}$, maroon, top) and nitrate (NO_3 , $\mu\text{mol kg}^{-1}$, blue, middle and
 1511 bottom) concentration (right axis during January through April for 2018 (top), 2019 (middle) and
 1512 2020 (bottom)).

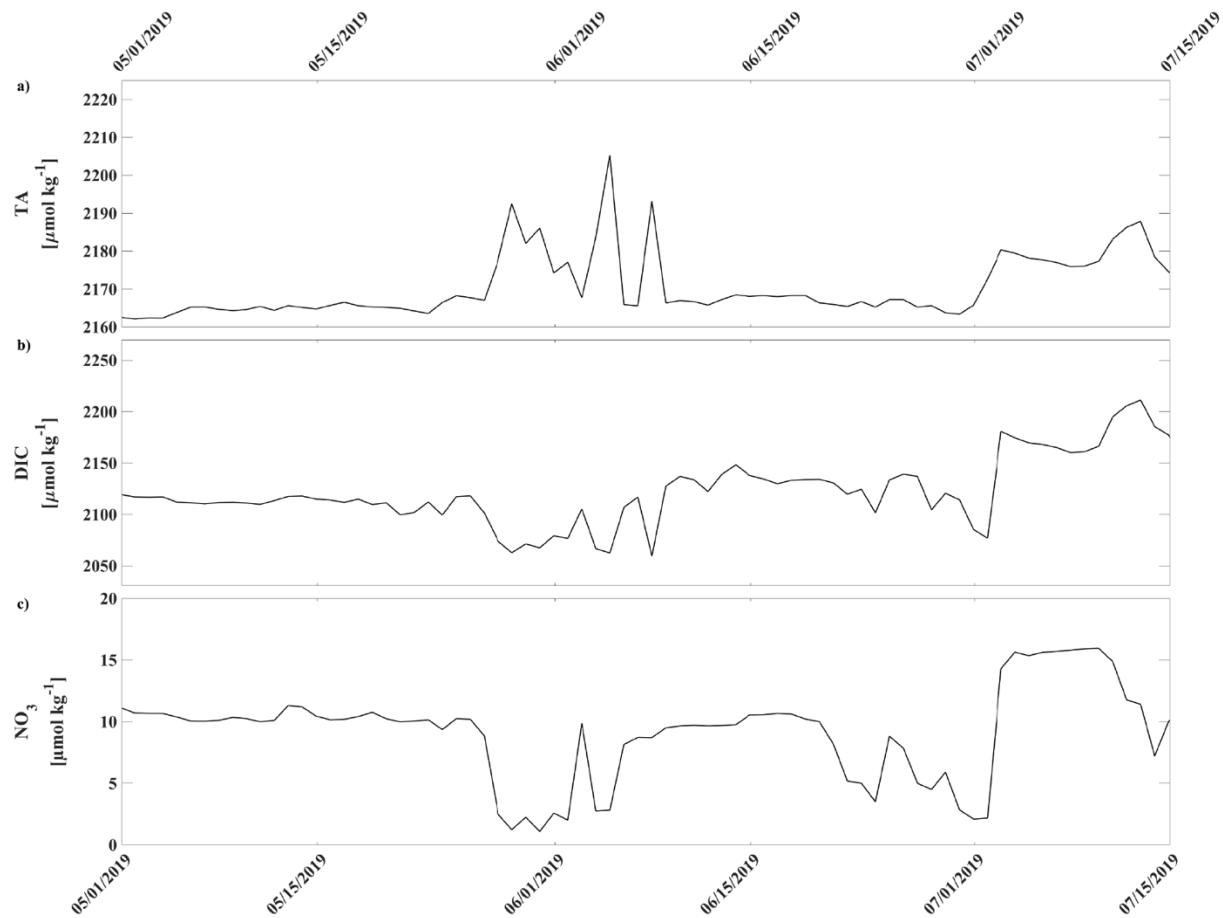
1513



1514

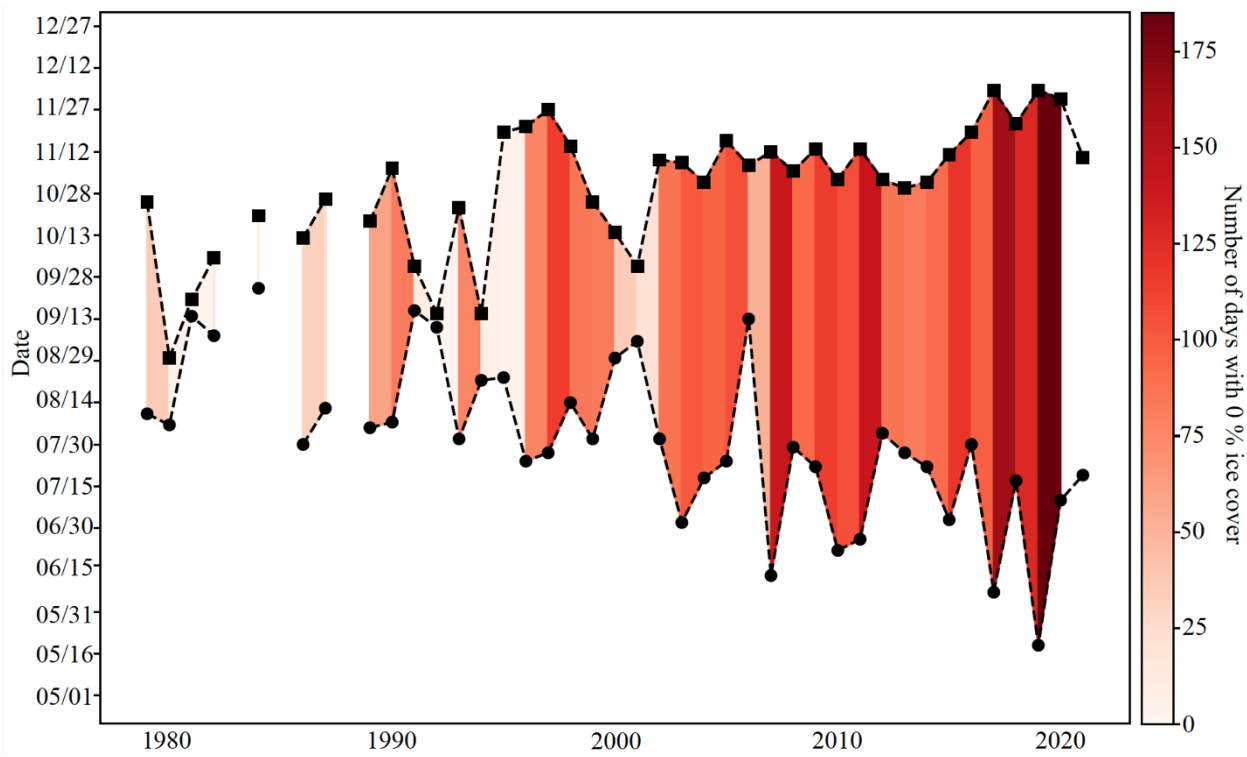
1515 **Figure 10. Drivers of the inorganic carbon system.** Component timeseries of the linear Taylor
 1516 decomposition of a) pH, b) Ω_{arag} , and c) $p\text{CO}_2$. The perturbation effects due to salinity (red),
 1517 temperature (blue), biogeochemistry (pink), and freshwater mixing (green), and an estimated
 1518 residual term (grey) were computed following Rheuban et al. (2019). Sea ice concentration (blue
 1519 shading, %; DiGirolamo et al., 2022) is shown on the right axes.

1520



1521

1522 **Figure 11. Spring 2019 relaxation event.** Timeseries of a) total alkalinity (TA, $\mu\text{mol kg}^{-1}$), b)
 1523 dissolved inorganic carbon (DIC, $\mu\text{mol kg}^{-1}$), and c) nitrate (NO_3 , $\mu\text{mol kg}^{-1}$) from May 1st, 2019
 1524 through July 15th, 2019.



1525

1526

1527 **Figure 12. Low sea ice period at the Chukchi Sea Observatory.** Timeseries of start (circle)
 1528 and end (square) of low sea ice (< 15 % per grid cell) period from 1982-2021. Shades of red
 1529 illustrate number of days with 0 % sea ice cover. The satellite sea ice cover at the observatory
 1530 site was taken from the NSIDC (DiGirolamo et al., 2022).

1531